Two-Parameter Identification Method of Deadtime Effect Voltage Error Model During Self-Commission

Danqi Xiang, *Student Member, IEEE*, Jianzhong Yang, Yong Hao, *Student Member, IEEE*, and Guangda Xu

***Abstract*—An identification method is presented for the arctan two-parameter model, which describes the deadtime effect voltage error of permanent magnet synchronous motor drives' three-phase voltage source inverter (VSI) during self-commission. In this method, the motor maintains a standstill during the whole identification process. First, a disturbance observer is used to improve the tracking performance of the total voltage error. Then, a technique is used to extract the deadtime effect voltage error from the total voltage error without a voltage sensor during the standstill condition. Finally, the core algorithm (utilizing the bisection method) is developed to solve the coupling problem in the two-parameter identification process, such that the parameters in the model converge simultaneously. Furthermore, a sufficient condition for the convergence of the algorithm is given, and a mathematical proof is presented. Experimental results show that the deadtime effect voltage error estimated by our method is closer to the measured voltage error than other state-of-the-art methods proposed in the literature.**

***Index Terms*—Bisection method, deadtime effect voltage error (DEVE), permanent magnet synchronous motor (PMSM), self-commission, standstill, two-parameter identification, voltage source inverter (VSI).**

I. Introduction

In THE past few decades, the permanent magnet synchronous motor (PMSM) has received extensive attention due to its merits of a simple structure, high efficiency, and high-power density. Due to these outstanding characteristics, PMSM has been widely applied in many industrial applications, such as robotics, electric vehicles, and computer numerical control machines.

The operation of a PMSM requires a servo drive system, and the performance of the controllers in a system with a high dynamic response depends on the accuracy of the motor's electrical parameters [1]. Therefore, the self-commission of PMSMs is indispensable for universal drive applications executed before motor startup. Normally, universal PMSM drives are not equipped with extra hardware to sample voltages, which are important to the identification of the motor's electrical parameters. In these servo drives, command voltages are common substitutes. Widely, a PMSM drive system is fed by a three-phase voltage source inverter (VSI). However, a deadtime interval is deployed in pulsewidth modulation (PWM) switching signals to prevent dc bus shorts caused by the turn-ON/OFF delay times of power switches. Therefore, the output voltages of inverters are different from the command voltages, resulting in voltage distortion, which is also called deadtime effect voltage error (DEVE). DEVEs can seriously deteriorate the accuracy of parameter identifications. Thus, the compensation of DEVEs has been an emerging demand for universal drive applications during self-commission.

Prior efforts have showed methods to compensate for DEVEs. These methods can be divided into passive compensation or active compensation. Passive compensation methods are usually used to suppress current harmonics generated during motor operation and then to reduce torque ripples [2], [3], [4], [5], [6], [7]. However, they cannot directly obtain DEVEs and, therefore, cannot be applied in motor parameter identifications during self-commission.

The active compensation methods can also be referred to as model-based methods when the look-up table is regarded as a special model. These model-based methods can be further divided into two categories. The first includes building an accurate inverter model. The authors in [8] and [9] used complex multiparameter models to describe the DEVE. However, these methods require offline data processing and are difficult to deploy to universal drives. The second includes a two-parameter model to describe the DEVE, which has been widely studied because of its ease of implementation. These models usually use the shape parameter to describe the effect of parasitic parameters [10], [11] when the phase current is at a low level and the plateau voltage to describe the saturation characteristic of the DEVE when the phase current is at a high-level. Arctan, tanh, and other two-parameter models are commonly used to describe the DEVE. Shan et al. [12] noted that using the arctan model can establish a stable mathematical and physical relationship.

A parameter identification process is required prior to using two-parameter models. Unfortunately, the capabilities to identify each individual parameters are coupled [13]. The authors in [14], [15], and [16] neglected the parasitic parameter effect and only use the plateau voltage to construct a square wave to solve the coupling. However, these methods are ineffective at compensating when the phase current is at a low level. The authors in [12] and [17] assumed that one of the parameters

Manuscript received 17 April 2023; revised 6 July 2023; accepted 18 August 2023. Date of publication 24 August 2023; date of current version 23 October 2023. This work was supported by the National Center of Technology Innovation for Intelligent Design and Numerical Control. Recommended for publication by Associate Editor I. S.-Belkhodja. *(Corresponding author: Guangda Xu.)*

The authors are with the Department of Mechanical Engineering, Huazhong University of Science and Technology, Wuhan 430074, China (e-mail: xiangdanqi60@gmail.com; yangjz@mail.hust.edu.cn; hao_yong@hust.edu.cn; xu_guangda@hust.edu.cn).

Color versions of one or more figures in this article are available at https://doi.org/10.1109/TPEL.2023.3308291.

Digital Object Identifier 10.1109/TPEL.2023.3308291

TABLE I
SUMMARY OF DIFFERENT TWO-PARAMETER DEVE MODELS

Method	Voltage error model	Unknown parameter(s)	Order of parameter identification	Standstill	Look-up table	Offline measured voltage error	Motor parameter sensitivity	Online estimation
[18], [19]	$V_{\mathrm{dt}} \tanh\left(\frac{K}{2} i_x\right)$	V_{dt}, K	$V_{\mathrm{dt}} \rightarrow K$	No	Not required	Not required	No	No
[13]	$V_{\mathrm{dt}} \tanh\left(\frac{K}{2} i_x\right)$	V_{dt}, K	$V_{\mathrm{dt}} \rightarrow K$	No	Not required	Not required	Yes	Yes
[17]	$\frac{2}{\pi} V_{\mathrm{dt}} \arctan\left(K i_x\right)$	V_{dt}	-	No	Not required	Not required	No	Yes
[12]	$\frac{2}{\pi} V_{\mathrm{dt}} \arctan\left(K i_x\right)$	K	-	No	Not required	Not required	No	No
[14], [15], [16]	Square wave	V_{dt}	-	-	Not required	Not required	No	-
[20], [21]	Trapezoidal wave	V_{dt}, K	$V_{\mathrm{dt}} \rightarrow K$	No	Not required	Not required	No	No
[22], [23], [24]	Saturation and look-up table	V_{dt}	-	Yes	Required	Not required	No	No
[25]	Adjust compensation time	t_{com}	-	Yes	Not required	Required	No	No
proposed method	$\frac{2}{\pi} V_{\mathrm{dt}} \arctan\left(K i_x\right)$	V_{dt}, K	Simultaneously	Yes	Not required	Not required	No	No

has been obtained accurately, and the other parameter needs to be identified. However, it is difficult to obtain an accurate known parameter. The authors in [13], [18], [19], [20], [21], [22], [23], and [24] identified the two parameters separately to avoid the coupling problem. Chen et al. [13] identified parameters online, but the process of the identification used motor parameters, which conflicts with the purpose of self-commission. The authors in [18], [19], [20], [21], [22], [23], and [24] used the most popular theory of nonlinear equivalent resistance during self-commission [24]. These methods first identify the plateau voltage and then the shape parameter. There are two limitations to these methods. The first is that they require the injection current to be large enough to let the DEVE reach the saturation region. If the deadtime is relatively long, the current level required for saturation of the DEVE may be much larger than the rated current of the motors. The second is that these methods usually identify the DEVE in the *dq*-frame, and it is difficult to project it to the *abc*-frame, which is more general (conversion from the *dq*-frame to the *abc*-frame is rank deficient [23]). That first limitation is inherent to the theory of operation, and no effective solution has yet been proposed (to the best of authors' knowledge). To alleviate that second limitation, the authors in [20] and [21] used different trapezoid waves to describe the transition region of the DEVE for each phase, and the shape parameter, the trapezoidal angle, needs to be identified under the condition of motor rotation. However, trapezoid waves have difficulty fitting the practical DEVE curve accurately. The authors in [18] and [19] described the DEVE using a tanh model, and the acquisition of the shape parameter is the same as [21]. The authors in [22], [23], and [24] used a look-up table to record the DEVE in the transition region on the *dq*-frame. However, it is complicated to convert to the *abc*-frame because the zero-axis voltage should be considered [23]. These aforementioned methods and some other special methods (which are not mentioned in detail) are summarized in Table I.

Typically, the electromotive force (EMF) of a PMSM is a nonideal sine wave that includes harmonics. When the motor is not stationary, its nonideal sinusoidal EMF will introduce corresponding errors to the parameter identification results of the DEVE. In addition, motors are usually connected to actuators before startup. Therefore, it is safer to keep motors in a standstill state than a rotating state for self-commission. However, it is easier to separate the DEVE from command voltages by the characteristic current harmonics [6] caused by injecting the deadtime when the motor is rotating.

Here, we use an arctan model to describe the DEVE and propose a method to identify the two parameters of the model. This method can accurately extract the DEVE from command voltages and solve the coupling problem of parameter identification. The main contributions of this article are as follows.

1) The proposed method can obtain the DEVE curve, which contains both transition and saturation regions, in the *abc*-frame when the motor is kept at standstill. This mitigates the effect of the nonstandard sinusoidal EMF of motors.
2) The proposed method can accurately extract the specific harmonic of the DEVE from the command voltages without any voltage sensor for identifying the parameters when the motor remains standstill, and it is insensitive to the motor electrical parameters. In addition, it does not require the currents to reach the level needed for the saturation of the DEVE.
3) Combined with the bisection method, the core algorithm of the proposed method can identify the two parameters of the arctan model simultaneously to solve the coupling problem. It does not require any offline data processing. A sufficient condition for the convergence of this algorithm and the corresponding proof are provided.

Experiment results demonstrate that the DEVE estimated by our method can describe the practical DEVE more accurately than state-of-the-art methods proposed in the literature.

The rest of this article is organized as follows. Section II presents the mathematical models of the PMSM drive system and the challenges faced when identifying the parameters. Section III presents a technique for obtaining the total voltage

error, a technique for separating the DEVE, and an algorithm for identifying the plateau voltage. They are the basis for the two-parameter identification. Section IV presents the core algorithm of the proposed method for simultaneously identifying the two parameters and proves the convergence of the algorithm. Section V reports experiments conducted to verify the proposed method and compares our method with competing approaches shown in the literature. Finally, Section VI concludes this article.

II. Mathematical Models

We assume that the employed PMSM has negligible cross-coupling magnetic saturation, structural asymmetry, iron losses, magnet eddy current loss, and harmonics in the descriptive functions of windings, rotor anisotropy, and coercive force of magnets [26]. The voltage equations of PMSM in the *dq*-frame are expressed as

$$\begin{cases} u_d = L_d \dfrac{\mathrm{d}i_d}{\mathrm{d}t} + Ri_d - \dfrac{p}{2}\omega_r L_q i_q \\ u_q = L_q \dfrac{\mathrm{d}i_q}{\mathrm{d}t} + Ri_q + \dfrac{p}{2}\omega_r L_d i_d + \dfrac{p}{2}\omega_r \psi_f \end{cases} \tag{1}$$

where u_d, u_q, i_d, i_q, L_d, L_q, R, ψ_f, ω_r, and p are the stator voltage, current and inductance, stator resistance, flux linkage generated by the rotor's permanent magnet, the rotational speed in mechanical angle, and the motor poles on the *dq*-frame, respectively.

Considering the uncertainties of the motor parameters and the nonideal characteristics of the inverter, the extended voltage equations of the PMSM are

$$\begin{cases} u_d = L_d \dfrac{\mathrm{d}i_d}{\mathrm{d}t} + Ri_d - \dfrac{p}{2}\omega_r L_q i_q + f_d \\ f_d = f_{d,\text{param}} + f_{d,\text{inv}} \end{cases}$$

$$\begin{cases} u_q = L_q \dfrac{\mathrm{d}i_q}{\mathrm{d}t} + Ri_q + \dfrac{p}{2}\omega_r L_d i_d + \dfrac{p}{2}\omega_r \psi_f + f_q \\ f_q = f_{d,\text{param}} + f_{d,\text{inv}} \end{cases} \tag{2}$$

where f_d and f_q represent voltage errors, including parameter errors and inverter voltage errors. $f_{d,\text{inv}}$ and $f_{q,\text{inv}}$ are inverter voltage errors in the *dq*-frame. while $f_{d,\text{param}}$ and $f_{q,\text{param}}$ are parameter voltage errors in the *dq*-frame and can be expressed as

$$\begin{cases} f_{d,\text{param}} = \Delta L_d \dfrac{\mathrm{d}i_d}{\mathrm{d}t} + \Delta R i_d - \dfrac{p}{2}\omega_r \Delta L_q i_q \\ f_{q,\text{param}} = \Delta L_q \dfrac{\mathrm{d}i_q}{\mathrm{d}t} + \Delta R i_q + \dfrac{p}{2}\omega_r \Delta L_d i_d + \dfrac{p}{2}\omega_r \Delta \psi_f \end{cases} \tag{3}$$

where ΔL_d, ΔL_q, ΔR, and $\Delta \psi_f$ are inductance uncertainty on the *d*-axis, inductance uncertainty on the *q*-axis, resistance uncertainty, and flux linkage uncertainty, respectively.

Inverter voltage errors are mainly characterized relative to the deadtime interval of power switches and the on-state voltages of semiconductor devices [17]. DEVEs and on-state voltages cause the output voltages of inverters to become different from the command voltages. The on-state voltages of power switches and freewheel diodes can be found in datasheets. The DEVE

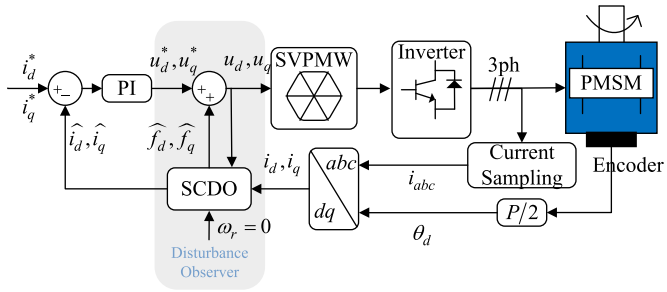

Fig. 1. Diagram of an SCDO-based PI current controller.

is affected by various factors, such as deadtime intervals, turn-ON/OFF delay times, parasitic parameters, and the bus voltage, so it needs to be identified.

Considering the influence of parasitic capacitance, the DEVE in each phase is expressed as

$$v_{\text{dt},x} = (2V_{\text{dt}}/\pi) \cdot \arctan(Ki_x), \qquad x = a, b, c \tag{4}$$

where i_x is the current in the x-phase, and the subscript x means a specific phase of PMSMs. $v_{\text{dt},x}$ comes from the deadtime effect and is modeled by two parameters, shape parameter K, and plateau voltage V_{dt}.

From (2) and (4), some coupling problems will arise when identifying the parameters of the arctan DEVE model.

1) It is difficult to separate the inverter voltage errors from the parameter voltage errors in (2) without any voltage sensor.
2) From (4), $v_{\text{dt},x}$ is determined by both V_{dt} and K and grows with them. Two parameters are coupled with each other during the identification.

Our method simultaneously identifies the two parameters in (4) during self-commission while the motor is kept at standstill. In addition, it accurately extracts the third harmonic of the practical DEVE without any voltage sensor to identify the parameters.

III. Premises of Two-Parameter Identification

This section introduces the following:

1) a technique to observe the total voltage error without any external circuit;
2) a technique to extract the DEVE from the total voltage error;
3) an identification algorithm of the plateau voltage when the shape parameter is determined.

These methods are the basis of the two-parameter simultaneous identification algorithm introduced in the following section.

A. Technique I: Observation of Total Voltage Error

The prerequisite for obtaining an accurate DEVE is to obtain an accurate total voltage error. A stator current disturbance observer (SCDO) [27] is used to estimate the total voltage errors in (2) without any voltage sensor.

SCDO is a widely-used technique to eliminate the one-step delay [28] in digital systems to improve the tracking performance for current commands. The outputs of an SCDO are the predicted currents and voltage errors. A sliding-mode-based

SCDO is used to track the voltage errors. The diagram of an SCDO-based current controller is shown in Fig. 1.

Remark 1: The SCDO used here not only serves as an observer to obtain the total voltage error but also improves the dynamic tracking performance for current commands.

According to (2), the extended voltage equations of the PMSM is expressed as

$$\begin{cases} u_d &= L_d\dfrac{\mathrm{d}i_d}{\mathrm{d}t} + Ri_d - \dfrac{p}{2}\omega_r L_q i_q + f_d \\ \dfrac{\mathrm{d}f_d}{\mathrm{d}t} &= F_d \end{cases}$$
$$\begin{cases} u_q &= L_q\dfrac{\mathrm{d}i_q}{\mathrm{d}t} + Ri_q + \dfrac{p}{2}\omega_r L_d i_d + \dfrac{p}{2}\omega_r\psi_f + f_q \\ \dfrac{\mathrm{d}f_q}{\mathrm{d}t} &= F_q \end{cases} \tag{5}$$

where F_d and F_q are the variation rates of f_d and f_q, respectively.

If the currents in the next control period are predicted accurately, then the voltage errors in (5) can be constructed simultaneously. The SCDO is, thus, designed as

$$\begin{cases} u_d = L_d\dfrac{\mathrm{d}\widehat{i_d}}{\mathrm{d}t} + R\widehat{i_d} - \dfrac{p}{2}\omega_r L_q i_q + \widehat{f_d} + U_{d\mathrm{smo}} \\ \dfrac{\mathrm{d}\widehat{f_d}}{\mathrm{d}t} = g_d U_{d\mathrm{smo}} \end{cases}$$
$$\begin{cases} u_q = L_q\dfrac{\mathrm{d}\widehat{i_q}}{\mathrm{d}t} + R\widehat{i_q} + \dfrac{p}{2}\omega_r L_d i_d + \dfrac{p}{2}\omega_r\psi_f + \widehat{f_q} + U_{q\mathrm{smo}} \\ \dfrac{\mathrm{d}\widehat{f_q}}{\mathrm{d}t} = g_q U_{q\mathrm{smo}} \end{cases} \tag{6}$$

where u_d and u_q represent the command voltages, and $\widehat{f_d}$, $\widehat{f_q}$, $\widehat{i_d}$, and $\widehat{i_q}$ represent the estimates of f_d, f_q, i_d, and i_q, respectively. $U_{d\mathrm{smo}}$ and $U_{q\mathrm{smo}}$ are sliding-mode control functions. g_d and g_q are larger than 0. If the following conditions:

$$\begin{cases} U_{d\mathrm{smo}} = (L_d\lambda - R)e_1 + k\cdot L_d\cdot \mathrm{sign}(e_1) \\ U_{q\mathrm{smo}} = (L_q\lambda - R)e_2 + k\cdot L_q\cdot \mathrm{sign}(e_2) \end{cases} \tag{7}$$

are met, the exponential reaching law can satisfy [27], and $\widehat{f_d}$ and $\widehat{f_q}$ will converge to f_d and f_q, respectively. e_1, e_2 are current estimation errors, $e_1 = \widehat{i_d} - i_d$, $e_2 = \widehat{i_q} - i_q$. λ and k are the parameters of the sliding-mode control. The analysis of the stability of the SCDO and the discrete form of the SCDO are presented in Appendices A and B. The estimation of the total voltage error on the d-axis, $\widehat{f_d}$, can be obtained from (40).

Remark 2: SCDO is a passive compensation method. There are several flaws if the voltage error observed by SCDO is directly treated as the DEVE when identifying motor parameters during self-commission: 1) including parameter voltage errors, so it cannot be used to identify motor parameters, and 2) poor voltage error tracking performance when high frequency current commands are injected.

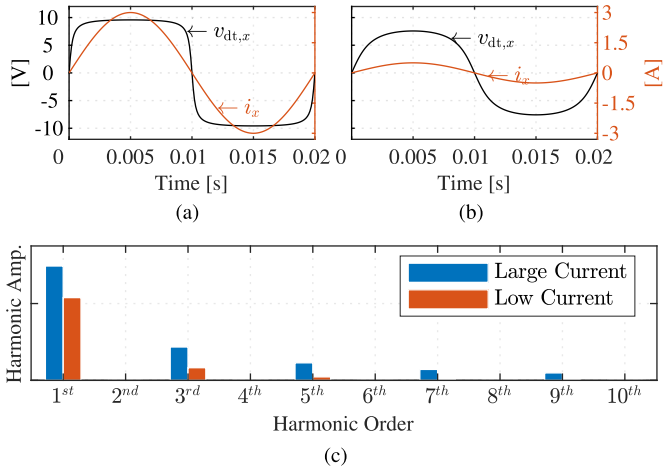

Fig. 2. (a) DEVE on the x-phase when the phase current is $i_x = 3\sin(100\pi t)$. (b) DEVE on the x-phase when the phase current is $i_x = 0.5\sin(100\pi t)$. (c) Harmonic analysis of the DEVEs at different phase currents.

B. Technique II: Extraction of DEVE on the D-Axis

The current injection method [29] is chosen to separate the DEVE from other voltage errors. The current on the q-axis is 0 to keep the motor standstill during self-commission, while a sinusoidal current, $i_d^* = I\sin(\omega t)$, is injected to the d-axis. Choosing the appropriate ω to satisfy the condition $\omega \ll \omega_c$ and using an SCDO-based current controller can ensure accurate tracking of current commands $i_d \approx i_d{}^*$. ω_c is the bandwidth of the current controller. Assuming that the electrical angle of the rotor is θ_d, the currents in the *abc*-frame are

$$\begin{cases} i_a = I\sin(\omega t)\cos(\theta_d) \\ i_b = I\sin(\omega t)\cos(\theta_d - 2\pi/3) \\ i_c = I\sin(\omega t)\cos(\theta_d - 4\pi/3). \end{cases} \tag{8}$$

In (8), the currents in the *abc*-frame are all sinusoidal, with the amplitude of each phase related to θ_d. The phases of the currents are 0 or π, and they are also related to θ_d. According to (4), when the phase current varies sinusoidally, $i_x = I_x\sin\omega_x t$, the DEVEs of each phase are shown in Fig. 2(a) and (b). Fig. 2(c) shows that the DEVE modeled by the arctan model consists of only odd-order harmonics. In the second half of this article, the third harmonic of the voltage error on the d-axis is used as a characteristic to identify the parameters of the DEVE model in the *abc*-frame.

Remark 3: There are two reasons to choose the third harmonic. First, when the injected signal is sinusoidal, according to (2), there are voltage errors caused by parameter uncertainties in the fundamental harmonic. Second, according to Fig. 3 , the third harmonic has a large amplitude and a higher signal-to-noise ratio compared to the higher odd harmonics.

Equation (4) shows that the amplitude of $v_{\mathrm{dt},x}$ is proportional to V_{dt}. Thus, the amplitude of the third harmonic of $v_{\mathrm{dt},x}$ is also proportional to V_{dt}. According to (4) and (8), the phase of the third harmonic of $v_{\mathrm{dt},x}$ is related to the sign of $\cos(\theta_d)$, $\cos(\theta_d - 2\pi/3)$ or $\cos(\theta_d - 4\pi/3)$. The third harmonic of the DEVE in

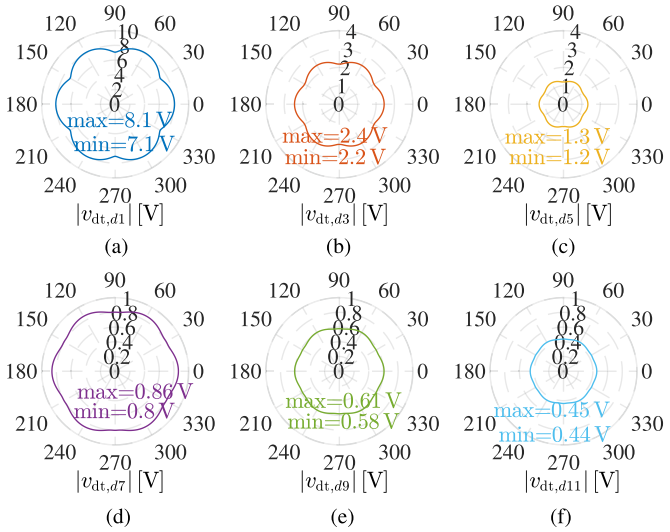

Fig. 3. Amplitudes of the odd harmonics of the DEVE on the d-axis for different θ_d when the injected current is $i_d^* = 3\sin(100\pi t)$ and $v_{dt,x} = (20/\pi)\arctan(10 i_x)$. (a) First harmonic. (b) Third harmonic. (c) Fifth harmonic. (d) Seventh harmonic. (e) Ninth harmonic. (f) 11th harmonic.

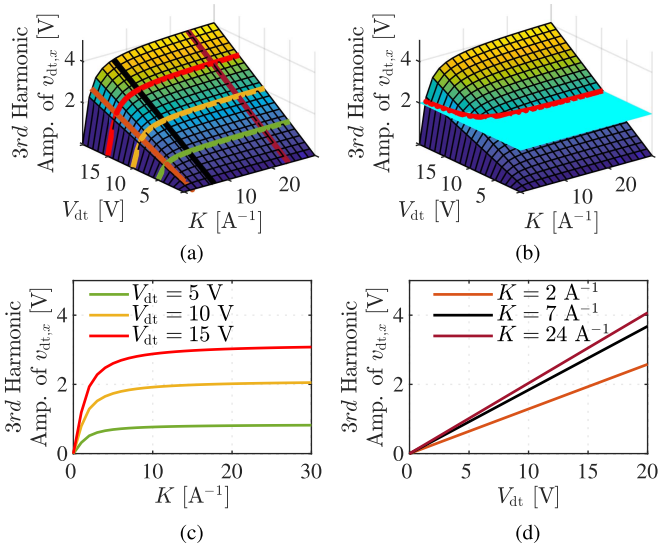

Fig. 4. Simulation results of the DEVE described in (4). (a) DEVE's third harmonic amplitude versus V_{dt} and K. (b) Same $v_{dt,x}$ corresponds to multiple combinations of V_{dt} and K. (c) $v_{dt,x}$ versus K when V_{dt} is constant. (d) $v_{dt,x}$ versus V_{dt} when K is constant.

the *abc*-frame is expressed as

$$\begin{cases} v_{dt,a3} = V_{dt} \cdot A_{3,a} \cdot \sin(3\omega t) \cdot \text{sign}\left(\cos\left(\theta_d\right)\right) \\ v_{dt,b3} = V_{dt} \cdot A_{3,b} \cdot \sin(3\omega t) \cdot \text{sign}\left(\cos\left(\theta_d - 2\pi/3\right)\right) \\ v_{dt,c3} = V_{dt} \cdot A_{3,c} \cdot \sin(3\omega t) \cdot \text{sign}\left(\cos\left(\theta_d - 4\pi/3\right)\right) \end{cases} \tag{9}$$

where $A_{3,x}$ is the amplitude coefficient of the DEVE in the *abc*-frame. When ω, I, θ_d, and K are constant, $A_{3,x}$ is constant. The third harmonic of the DEVE on the d-axis is

$$\begin{aligned} v_{dt,d3} &= \frac{2}{3}\left[v_{dt,a3}\cos\left(\theta_d\right) + v_{dt,b3}\cos\left(\theta_d - 2\pi/3\right)\right. \\ &\quad \left. + v_{dt,c3}\cos\left(\theta_d - 4\pi/3\right)\right] \\ &= \frac{2}{3}V_{dt}\left[\underbrace{A_{3,a}\cdot\left|\cos(\theta_d)\right|}_{C_a} + \underbrace{A_{3,b}\cdot\left|\cos(\theta_d - 2\pi/3)\right|}_{C_b}\right. \\ &\quad \left. + \underbrace{A_{3,c}\cdot\left|\cos(\theta_d - 4\pi/3)\right|}_{C_c}\right]\cdot\sin\left(3\omega t\right) \\ &= \frac{2}{3}V_{dt}\left(C_a + C_b + C_c\right)\sin\left(3\omega t\right). \end{aligned} \tag{10}$$

When ω, I, K, and θ_d are constant, C_a, C_b, and C_c are constant. The amplitudes of the first, third, fifth, seventh, ninth, and 11th harmonics of the DEVE on the d-axis versus θ_d are shown in Fig. 3 when ω, I, and K are constant. The amplitude of the third harmonic is always nonzero.

The back EMF of a PMSM is zero under the stationary condition [21], so the harmonics of the EMF are not introduced into the total voltage error. Therefore, parameter voltage errors only affect the fundamental harmonic of the total voltage error. Thus, the third harmonic of the total voltage error on the d-axis is entirely attributed to $f_{d,\text{inv}}$. The on-state voltages of semiconductor devices are obtained from datasheets and can be compensated directly. Here, $f_{d,\text{inv}}$ is equivalent to the DEVE on the d-axis. Therefore, the third harmonic of the total voltage error on the d-axis is selected as a characteristic of the DEVE.

First, an auxiliary signal, $i_{d,3} = \sin(3\omega t)$, is constructed to extract the amplitude of $v_{dt,d3}$, and then $v_{dt,d3}$ is reconstructed. Using the orthogonality of trigonometric functions

$$\text{DC}\left(\sin\left(m\omega t\right)\cdot\sin\left(n\omega t\right)\right) = \begin{cases} 0, & m \neq n \\ 1/2, & m = n \end{cases} \tag{11}$$

where $\text{DC}(\cdot)$ denotes the dc component,

$$\text{DC}\left(v_{dt,d3}\cdot i_{d,3}\right) = \frac{1}{3}V_{dt}\left(C_a + C_b + C_c\right). \tag{12}$$

$v_{dt,d3}$ is included in the total voltage error on the d-axis, f_d. Thus

$$\text{DC}\left(f_d\cdot i_{d,3}\right) = \frac{1}{3}V_{dt}\left(C_a + C_b + C_c\right). \tag{13}$$

C. Algorithm I: Identification of V_{dt} for Given K

V_{dt} and K cannot be identified directly after obtaining $v_{dt,d3}$ through Technique I and Technique II. First, V_{dt} and K are the parameters of DEVE in the *abc*-frame, and $v_{dt,d3}$ is useful only if it is converted to $v_{dt,x}$. Second, there is a coupling between V_{dt} and K, which indicates that the same $v_{dt,x}$ corresponds to multiple combinations of V_{dt} and K, as shown in Fig. 4(b).

According to (10), when ω, I, K, and θ_d are constant, C_a, C_b, and C_c are constant, and $v_{dt,d3}$ is proportional to V_{dt}. Therefore, for any given K and injected current, $i_d^* = I\sin(\omega t)$, there always exists a V_{dt}, which is used to compensate for the DEVE by (4) to eliminate $v_{dt,d3}$. After compensation, the third harmonic of the voltage error on the d-axis reduces to zero.

Since C_a, C_b, and C_c vary with ω, I, K, and θ_d, V_{dt} cannot be calculated directly using (10). In this article, we use (4) to compensate the DEVE in the *abc*-frame and then use a

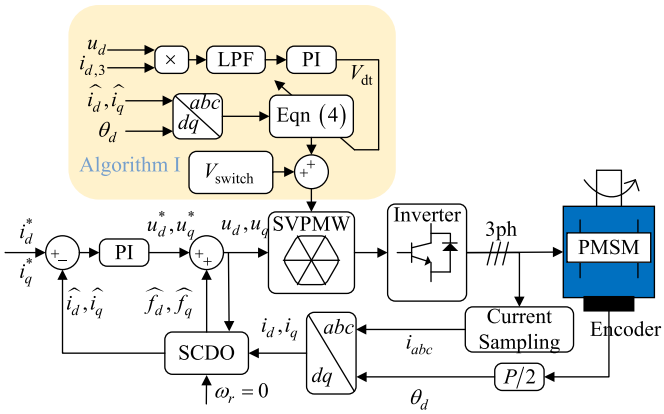

Fig. 5. Diagram of Algorithm I.

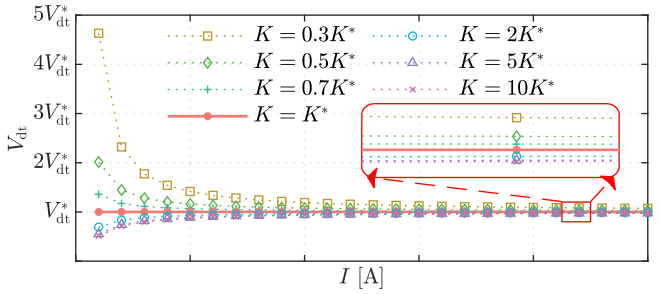

Fig. 6. Simulation results of $V_{\rm dt}$ identified by Algorithm I for different injected current amplitudes I on the d-axis.

proportional-integral regulator to tune $V_{\rm dt}$ online to eliminate the third harmonic of the voltage error on the d-axis. This method avoids the rank deficiency problem when $v_{{\rm dt},d3}$ is converted to $v_{{\rm dt},x}$. The diagram of the algorithm is shown in Fig. 5, where $V_{\rm switch}$ is the on-state voltage of the semiconductor devices, and the LPF in the figure is a low-pass filter.

Notably, if K equals the rated shape parameter of the DEVE model, K^*, keeping ω constant, the same $V_{\rm dt}$ is obtained regardless of I, and $V_{\rm dt} = V_{\rm dt}^*$. Conversely, different I gives different $V_{\rm dt}$, and this pattern can be found in Fig. 6. K^* and $V_{\rm dt}^*$ are the rated parameters of the DEVE model.

Remark 4: If $K \neq K^*$, the $V_{\rm dt}$ obtained by Algorithm I can only guarantee that the third harmonic of the DEVE on d-axis converted from the $v_{{\rm dt},x}$ in abc-frame is equal to the DEVE on d-axis converted from the $v_{{\rm dt},x}^*$, $v_{{\rm dt},x}^* = (2V_{\rm dt}^*/\pi)\arctan(K^* i_x)$, when the injected current is, $i_d{}^* = I\sin(\omega t)$. This property is denoted as (21) in the following section.

IV. Algorithm II: Identification of $V_{\rm dt}$ and K

There are two challenges in simultaneously obtaining $V_{\rm dt}$ and K by solving (4): 1) the rank deficiency problem and 2) the nonlinearity between $v_{{\rm dt},x}$ and K. Regarding the first, it is impossible to solve one equation to obtain two variables. Regarding the second, although the system of equations obtained by injecting different currents can solve the rank deficiency problem, obtaining the analytical solution of the system of equations is difficult.

This section, therefore, proposes an algorithm combining the bisection method and Algorithm I proposed in the last section to search K in the candidate interval. As K converges to K^*, $V_{\rm dt}$ converges to $V_{\rm dt}^*$ simultaneously. Additionally, this section provides a sufficient condition for the convergence of the algorithm and its corresponding proof. Suppose the candidate interval of K is $[K_1, K_2]$, and the accuracy of K is ξ. The flowchart of this algorithm is shown in Fig. 7.

We, thus, derive the convergence condition of Algorithm II and prove it. To better explain the proof, some notations are initially defined.

Suppose the rated parameters of the DEVE on the abc-frame are K^* and $V_{\rm dt}^*$. When the electrical angle of the rotor is θ_d and the injected current's amplitude is I, $V_{\rm dt}(K, I)$ can be obtained using Algorithm I for any K in $[K_1, K_2]$.

The part containing $V_{\rm dt}$ in (4) needs to be separated from the part containing K for further analysis. When the phase current is sinusoidal, the part containing K is defined as the basic element, which is expressed as

$$v(K, I) = \arctan\left(K \cdot I\sin(\omega t)\right). \tag{14}$$

Because the input current is periodic, the basic element is also periodic. Therefore, the basic element is expanded into a Fourier series to separate the coefficient of the third harmonic. The coefficient is expressed as

$$v_3(K, I) = \frac{2\pi}{\omega}\int_{-\frac{\pi}{\omega}}^{\frac{\pi}{\omega}} \arctan\left(K \cdot I\sin(\omega t)\right)\sin(3\omega t)\,{\rm d}t. \tag{15}$$

As shown in Fig. 7, Algorithm II combines Algorithm I and the bisection method to iteratively identify K and $V_{\rm dt}$ in the candidate interval. According to the convergence condition of the bisection method, it can be inferred that Algorithm II converges when the following three conditions are satisfied:

1) When $K \to K^*$, $1/V_{\rm dt}(K, mI) - 1/V_{\rm dt}(K, I) \to 0$.
2) $[(1/V_{\rm dt}(K_1, mI) - 1/V_{\rm dt}(K_1, I))$ $\times (1/V_{\rm dt}(K_2, mI) - 1/V_{\rm dt}(K_2, I))] < 0$.
3) $1/V_{\rm dt}(K, mI) - 1/V_{\rm dt}(K, I)$ varies monotonically with K.

Condition 1 can be inferred easily from Fig. 6. Condition 2 can be satisfied by choosing a suitable candidate interval. Only Condition 3 needs to be proven.

First, we prove some properties of the basic element.

Theorem 1: When $K > 0$, $I > 0$, then $v_3(K, I) > 0$, and $v_3(K, I)$ increases monotonically with K and I.

Proof: The partial derivative of $v_3(K, I)$ with respect to K is

$$\begin{aligned}\frac{\partial v_3(K, I)}{\partial K} &= \frac{2\pi}{\omega}\int_{-\frac{\pi}{\omega}}^{\frac{\pi}{\omega}} \frac{I\sin(\omega t)}{1 + K^2 I^2 \cdot \sin^2(\omega t)}\sin(3\omega t)\,{\rm d}t \\ &= \frac{8\pi}{\omega}\int_{0}^{\frac{\pi}{2\omega}} \frac{I\sin(\omega t)}{1 + K^2 I^2 \cdot \sin^2(\omega t)}\sin(3\omega t)\,{\rm d}t.\end{aligned} \tag{16}$$

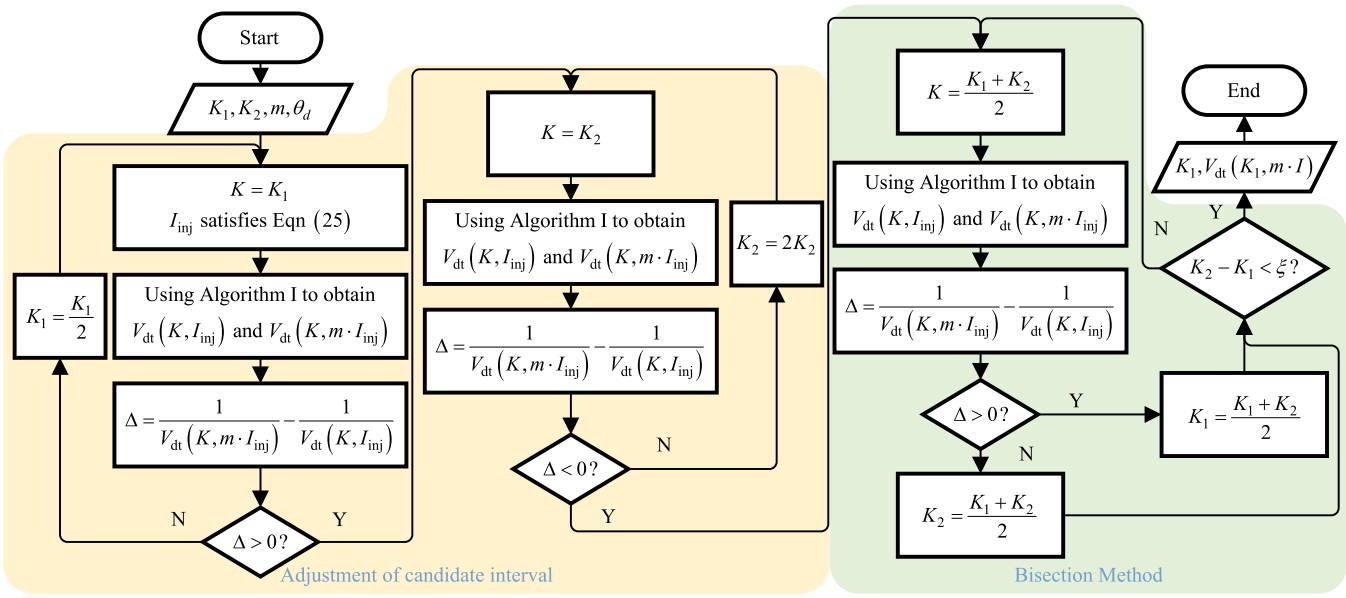

Fig. 7. Flowchart of Algorithm II.

When $t \in [0, \pi/2\omega]$, $I\sin(\omega t)/(1 + K^2 I^2 \sin^2(\omega t)) \geq 0$. Hence

$$\begin{cases} \frac{I\sin(\omega t)\sin(3\omega t)}{(1+K^2I^2\sin^2(\omega t))} \geq 0, & t \in [0, \pi/3\omega) \\ \frac{I\sin(\omega t)\sin(3\omega t)}{(1+K^2I^2\sin^2(\omega t))} \leq 0, & t \in [\pi/3\omega, \pi/2\omega]. \end{cases} \tag{17}$$

Substituting (17) into (16), then

$$\begin{aligned} \frac{\partial v_3(K,I)}{\partial K} &= \frac{8\pi}{\omega}\left[\int_0^{\frac{\pi}{3\omega}} \frac{I\sin(\omega t)}{1 + K^2I^2 \cdot \sin^2(\omega t)} \sin(3\omega t)\,\mathrm{d}t \right. \\ &\quad \left. + \int_{\frac{\pi}{3\omega}}^{\frac{\pi}{2\omega}} \frac{I\sin(\omega t)}{1 + K^2I^2 \cdot \sin^2(\omega t)} \sin(3\omega t)\,\mathrm{d}t\right] \\ &\geq \frac{8\pi}{\omega}\left[\int_0^{\frac{\pi}{3\omega}} \frac{I\sin(\omega t)}{1 + K^2I^2 \cdot \sin^2\left(\frac{\pi}{3}\right)} \sin(3\omega t)\,\mathrm{d}t \right. \\ &\quad \left. + \int_{\frac{\pi}{3\omega}}^{\frac{\pi}{2\omega}} \frac{I\sin(\omega t)}{1 + K^2I^2 \cdot \sin^2\left(\frac{\pi}{3}\right)} \sin(3\omega t)\,\mathrm{d}t\right] \\ &= \frac{8\pi}{\omega}\int_0^{\frac{\pi}{2\omega}} \frac{I\sin(\omega t)}{1 + K^2I^2 \cdot \sin^2\left(\frac{\pi}{3}\right)} \sin(3\omega t)\,\mathrm{d}t \\ &= 0. \end{aligned} \tag{18}$$

Only when $I = 0$, $\partial v_3(K,I)/\partial K = 0$. Hence, $v_3(K,I)$ increases monotonically with K, and $v_3(K,I) > v_3(0,I) = 0$. According to the equivalence of K and I in $v_3(K,I)$, $v_3(K,I)$ increases monotonically with I. ■

The numerical simulation results of $v_3(K,I)$ are shown in Fig. 8.

The derivations of $A_{3,a}$, $A_{3,b}$, and $A_{3,c}$ in (9) were omitted in the previous section and are now rederived. When the injected current on the d-axis is $i_d^* = I\sin(\omega t)$, the rotor's electrical angle is θ_d, and the currents in the abc-frame can be obtained from

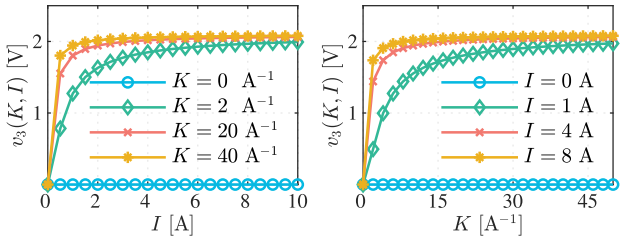

Fig. 8. Simulation results of the amplitude of $v_3(K,I)$ under different conditions. (a) $v_3(K,I)$ versus I under different K. (b) $v_3(K,I)$ versus K under different I.

(8). Combined with (15), we can obtain

$$\begin{cases} A_{3,a} = \frac{2}{\pi} \cdot v_3\left(K, I \cdot \left|\cos\left(\theta_d\right)\right|\right) \\ A_{3,b} = \frac{2}{\pi} \cdot v_3\left(K, I \cdot \left|\cos\left(\theta_d - \frac{2\pi}{3}\right)\right|\right) \\ A_{3,c} = \frac{2}{\pi} \cdot v_3\left(K, I \cdot \left|\cos\left(\theta_d - \frac{4\pi}{3}\right)\right|\right). \end{cases} \tag{19}$$

C_a, C_b, and C_c in (10) can be expressed as

$$\begin{cases} C_a = \frac{2}{\pi} \cdot \left|\cos\left(\theta_d\right)\right| \cdot v_3\left(K, I \cdot \left|\cos\left(\theta_d\right)\right|\right) \\ C_b = \frac{2}{\pi} \cdot \left|\cos\left(\theta_d - \frac{2\pi}{3}\right)\right| \cdot v_3\left(K, I \cdot \left|\cos\left(\theta_d - \frac{2\pi}{3}\right)\right|\right) \\ C_c = \frac{2}{\pi} \cdot \left|\cos\left(\theta_d - \frac{4\pi}{3}\right)\right| \cdot v_3\left(K, I \cdot \left|\cos\left(\theta_d - \frac{4\pi}{3}\right)\right|\right). \end{cases} \tag{20}$$

According to the previous section, $V_{dt}(K,I)$ obtained by Algorithm I can satisfy that the third harmonic of the estimated DEVE is equal to the third harmonic of the rated DEVE on the d-axis, i.e.,

$$\begin{aligned} &V_{dt}(K,I)\left[C_a(K,I) + C_b(K,I) + C_c(K,I)\right] \\ &\quad = V_{dt}^* \underbrace{\left[C_a\left(K^*,I\right) + C_b\left(K^*,I\right) + C_c\left(K^*,I\right)\right]}_{C_{3d}^*(I)}. \end{aligned} \tag{21}$$

Next, a sufficient condition will be derived to let Condition 3 hold.

Theorem 2: For any k in the closed interval $[K_1, K_2]$, where $0 < K_1 < K_2$, it is true that

$$V_{\mathrm{dt}}(k,I)\left[C_a(k,I)+C_b(k,I)+C_c(k,I)\right] = V_{\mathrm{dt}}^* C_{3d}^*(I) \tag{22}$$

$$V_{\mathrm{dt}}(k,mI)\left[C_a(k,mI)+C_b(k,mI)+C_c(k,mI)\right] = V_{\mathrm{dt}}^* C_{3d}^*(mI) \tag{23}$$

$$f(k) = \frac{1}{V_{\mathrm{dt}}(k,mI)} - \frac{1}{V_{\mathrm{dt}}(k,I)} \tag{24}$$

when $I > 0$, $m > 1$. If

$$I \geq \frac{5}{K_1 \cdot \min\left\{\left|\cos(\theta_d)\right|, \left|\cos\left(\theta_d - \frac{2\pi}{3}\right)\right|, \left|\cos\left(\theta_d - \frac{4\pi}{3}\right)\right|\right\}} \tag{25}$$

then

$$\frac{\partial}{\partial k} f(k) < 0. \tag{26}$$

Proof: (22) and (23) are substituted into (24), and then the derivative of $f(k)$ is calculated as

$$\begin{aligned}
&\frac{\partial}{\partial k} f(k) \\
&= \frac{\partial}{\partial k}\left\{\frac{\left[C_a(k,mI)+C_b(k,mI)+C_c(k,mI)\right]}{V_{\mathrm{dt}}^* C_{3d}^*(mI)} - \frac{\left[C_a(k,I)+C_b(k,I)+C_c(k,I)\right]}{V_{\mathrm{dt}}^* C_{3d}^*(I)}\right\} \\
&= \frac{1}{V_{\mathrm{dt}}^*}\left\{\left[\frac{\frac{\partial}{\partial k}C_a(k,mI)}{C_{3d}^*(mI)} - \frac{\frac{\partial}{\partial k}C_a(k,I)}{C_{3d}^*(I)}\right] + \left[\frac{\frac{\partial}{\partial k}C_b(k,mI)}{C_{3d}^*(mI)} - \frac{\frac{\partial}{\partial k}C_b(k,I)}{C_{3d}^*(I)}\right] + \left[\frac{\frac{\partial}{\partial k}C_c(k,mI)}{C_{3d}^*(mI)} - \frac{\frac{\partial}{\partial k}C_c(k,I)}{C_{3d}^*(I)}\right]\right\}.
\end{aligned} \tag{27}$$

Therefore, it is only necessary to prove that

$$\frac{\frac{\partial}{\partial k}C_x(k,mI)}{C_{3d}^*(mI)} - \frac{\frac{\partial}{\partial k}C_x(k,I)}{C_{3d}^*(I)} < 0, \qquad x = a,b,c. \tag{28}$$

Take the a-phase as an example, and the others can be proved in the same way. When $x = a$

$$\frac{\partial}{\partial k} C_a(k,I) = \frac{2\left|\cos(\theta_d)\right|}{\pi}\left(\frac{\partial}{\partial K} v_3(K,I)\Big|_{K=k, I=I\left|\cos(\theta_d)\right|}\right). \tag{29}$$

According to (18), $\partial v_3(K,I)/\partial K > 0$. According to Theorem 3 in Appendix C, $\partial v_3(K,I)/\partial K$ decreased monotonically with I when $I \geq 5/K$. Thus, when $I \geq 5/(K_1|\cos(\theta_d)|)$, $(\partial/\partial k)C_a(k,I) > (\partial/\partial k)C_a(k,mI) > 0$. According to Theorem 1, $C_{3d}^*(mI) > C_{3d}^*(I) > 0$. Then, (28) can be derived if $x = a$.

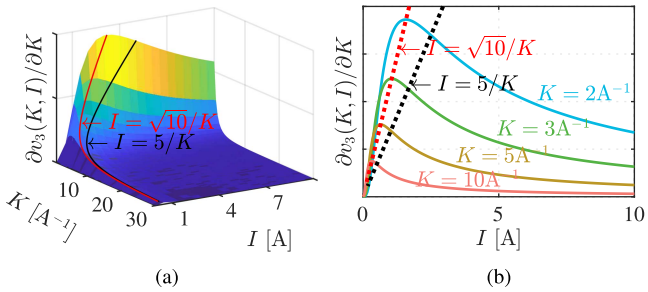

Fig. 9. Simulation results of $\partial v_3(K,I)/\partial K$. (a) $\partial v_3(K,I)/\partial K$ versus I and K. (b) Projection of the three-dimensional curve in (a) onto the plane $I - \partial v_3(K,I)/\partial K$.

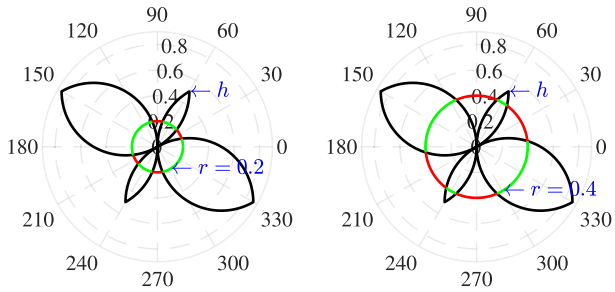

Fig. 10. Relationship between the denominator of the right-hand side in (25) $\min(\cdot)$ and θ_d. The green line indicates the area that meets the condition and the red line indicates the area that does not meet the condition.

Similarly, when I satisfies (25), (28) can be derived in the closed interval $[K_1, K_2]$ for $x = a, b, c$.

Finally

$$\frac{\partial}{\partial k} f(k) < 0. \tag{30}$$

■

Remark 5: According to Theorem 3, for any K in the candidate interval, the condition $I \geq 5/K$ can guarantee that $\partial v_3(K,I)/\partial K$ decreases monotonically with I, as shown in Fig. 9 . In fact, the proof of Theorem 3 uses a nontight bound obtained by inequality scaling. The numerical simulation results in Fig. 9 show that the condition $I \geq \sqrt{10}/K$ can guarantee that $\partial v_3(K,I)/\partial K$ decreases monotonically with I. The experimental part still uses the sufficient condition, $I \geq 5/K$.

Algorithm II lets (22) and (23) hold by using Algorithm I according to (21). Therefore, as long as the amplitude of the injected current on d-axis satisfies (25) within the candidate interval, $[K_1, K_2]$, then Condition 3 holds in the interval. Finally, Algorithm II converges, $K \to K^*$. According to Fig. 6, V_{dt} converges to V_{dt}^* when K converges to K^*. Two parameters converge simultaneously.

Remark 6: From (25), it can be seen that some θ_d will make the lower bound of I exceed the rated current of the PMSM. Generally, the parasitic capacitance is not very large, then K^* is not very small, and θ_d still has a wide range of choices. In Fig. 10 , h is the denominator of the right-hand side in (25), $\min(\cdot)$. It can be seen that θ_d has a wide range of choices (green line) when $h \geq 0.2$ or $h \geq 0.4$.

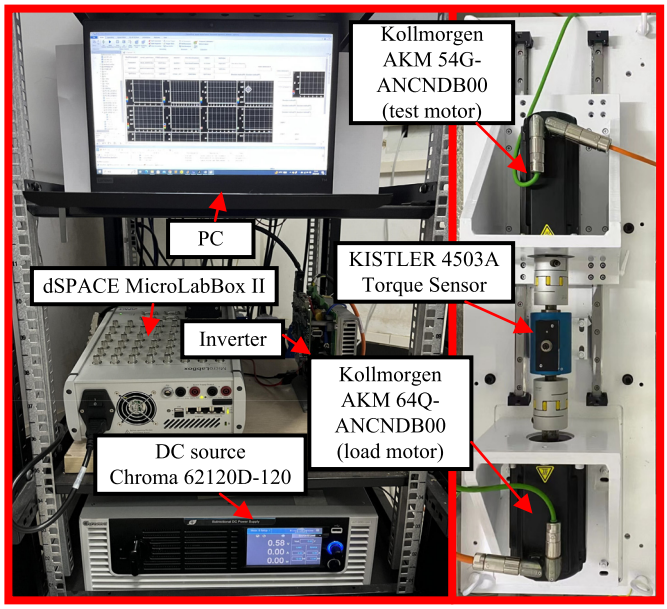

Fig. 11. Experiment platform.

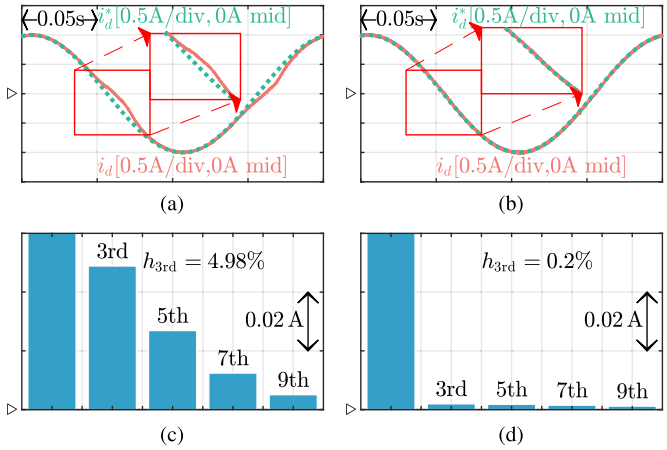

Fig. 12. Performance comparison of a PI current controller and an SCDO-based PI current controller when the injected current on the d-axis is $i_d^* = \sin(10\pi t)$. (a) Current tracking performance of the PI current controller. (b) Current tracking performance of the SCDO-based PI current controller. (c) Analysis of the current harmonics of the PI current controller. (d) Analysis of the current harmonics of the SCDO-based PI current controller. The hollow triangle in the figure indicates the 0 level, and h_{3rd} represents the ratio of the third harmonic's amplitude to the fundamental harmonic's amplitude.

TABLE II
PARAMETERS OF TEST PMSM

Symbol	Quantity	Value
p	Number of poles	10
R^*	Stator resistance (Ω)	2.16
L_d^*	Stator d-axis inductance (mH)	11
L_q^*	Stator q-axis inductance (mH)	11
ψ_f^*	Rotor flux linkage (Wb)	0.3004
J	Rotational Inertial ($\mathrm{Kg \cdot cm^2}$)	12

TABLE III
PARAMETERS OF IPM MITSUBISHI PSS30S71F6

Symbol	Quantity	Value
V_{DC}	Output voltage of dc power supply(V)	311
f_{sw}	Inverter switching frequency (Hz)	10 K
T_d	Dead time (μs)	4

V. EXPERIMENTS

A. Experimental Setup

In Fig. 11, an experiment platform was built to validate the proposed methods based on the PMSM, including parameters as summarized in Table II. An IGBT-based intelligent power module (IPM) is selected, and the parameters of the IPM are listed in Table III. The dSPACE MicroLabBox II in Fig. 11 is used to execute our methods.

B. Verification of SCDO's Performance on Voltage Error Tracking

By injecting a current signal into the d-axis and maintaining the current on the q-axis at 0, the rotor is kept at standstill. To ensure that SCDO accurately tracks the voltage error, the frequency of the injected current signal cannot be too large, $\omega = 10\pi$ rad/s. The parameters of SCDO are $\lambda = 1131$, $k = 220$, and $g_d = g_q = 34214$. The PI current controller and the SCDO-based PI current controller are configured with the same proportional and integral parameters. Their tracking performances for $i_d^* = \sin(\omega t)$ are compared in Fig. 12.

Fig. 12(a) and (b) shows that the SCDO-based PI current controller tracks the current command more accurately than the PI current controller for the same PI parameters, especially when currents cross zero. Based on Fig. 12(c) and (d), the SCDO-based PI current controller exhibits almost zero odd current harmonics, which indicates that the odd voltage errors are almost completely observed and compensated by SCDO. This condition is the prerequisite for Algorithms I and II to be valid.

TABLE IV
TRACKING PERFORMANCE OF DIFFERENT METHODS

Method	Roundtime	Third (A)	Fifth(A)	Seventh(A)
SCDO-PI	2.37 μs	5.5e−4	6.4e−4	6.0e−4
MFPCC-ESO	2.39 μs	1.8e−3	1.4e−3	1.1e−3
PI	2.34 μs	4.7e−2	2.8e−2	1.4e−2

Furthermore, we also compared them with the MFPCC-ESO [30]. When $i_d^* = \sin(10\pi t)$, their computational time consumption and the amplitude of current harmonics are listed in Table IV. Since MFPCC-ESO is not based on a PI control structure, we separately tuned the parameters of the three methods to minimize harmonics for comparison.

C. Verification of Algorithm I

This section verifies that Algorithm I can eliminate the third harmonic of the voltage error on the d-axis by tuning V_{dt} when the shape parameter, K, and the amplitude of the current injected on the d-axis, I, are determined. When $K = 11\ \mathrm{A}^{-1}$, $i_d^* = 5\sin(\omega t)$, and $\omega = 10\pi$ rad/s, Fig. 13 shows the process of using the method in Fig. 5 to tune V_{dt} so that the third harmonic of the voltage error observed by SCDO approaches 0. The moving

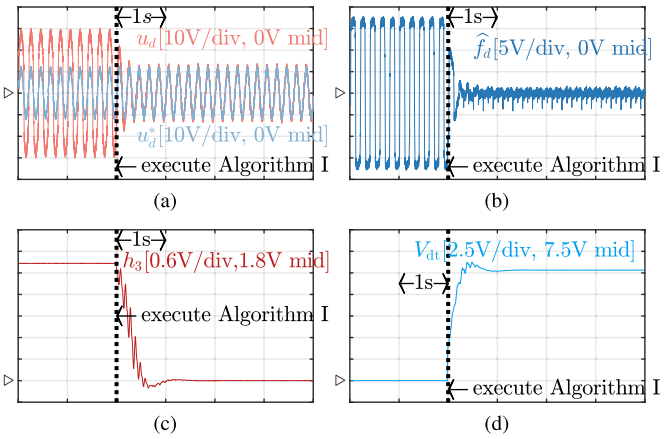

Fig. 13. Experimental verification of Algorithm I. (a) Trend of the output of the SCDO-based PI current controller, u_d, and u_d^*. (b) Trend of the total voltage error observed by SCDO. (c) Trend of the third harmonic of the total voltage error. (d) Trend of V_{dt}.

TABLE V
CONVERGENCE VALUES OF V_{dt} UNDER DIFFERENT CONDITIONS

Condition	V_{dt}(V)
$R = R^*, L = L^*$	12.77
$R = 0.5R^*, L = L^*$	12.75
$R = R^*, L = 0.5L^*$	12.76
$R = 2R^*, L = L^*$	12.76
$R = R^*, L = 2L^*$	12.76

average is chosen as the LPF in Fig. 5, and V_{switch} is obtained through the datasheet of the IPM.

According to Fig. 13(a), after executing Algorithm I, the output voltage of the SCDO-based PI current controller, u_d, continuously converges to u_d^*, which approximately equals the result calculated using the ideal voltage equations (1). According to Fig. 13(b) and (c), both the total voltage error observed by SCDO, $\widehat{f}_d$, and the third harmonic of the voltage error observed by SCDO, h_3, converge to 0.

To demonstrate that Algorithm I can decouple the DEVE from parameter voltage errors, different motor parameters are set for the given controller, as shown in Table V. When $K = 11\ \mathrm{A}^{-1}$, $i_d^* = 5\sin(\omega t)$, $\omega = 10\pi$ rad/s, V_{dt} converges to almost the same value. This finding indicates that there is almost no third harmonic in the parameter voltage errors, so Algorithm I can extract the clean DEVE from the total voltage error.

D. Verification of Algorithm II

This section shows the convergence process of Algorithm II, where $\xi = 0.1\ \mathrm{A}^{-1}$, $K_1 = 5\ \mathrm{A}^{-1}$, $K_2 = 15\ \mathrm{A}^{-1}$, and $\theta_d = 0$. To satisfy (25), $I \geq 5/|K_1 \cos(2\pi/3)| = 2\ \mathrm{A}$, $I = 2\ \mathrm{A}$, $m = 5$. The convergence of shape parameter K and plateau voltage V_{dt} are shown in Fig. 14. In the candidate interval $[K_1, K_2]$, K is selected using the bisection method and then used to obtain the V_{dt} under different amplitudes of the injected current by Algorithm I. Different V_{dt} are brought into (24), and the sign is judged to narrow the candidate interval. Finally, K converges

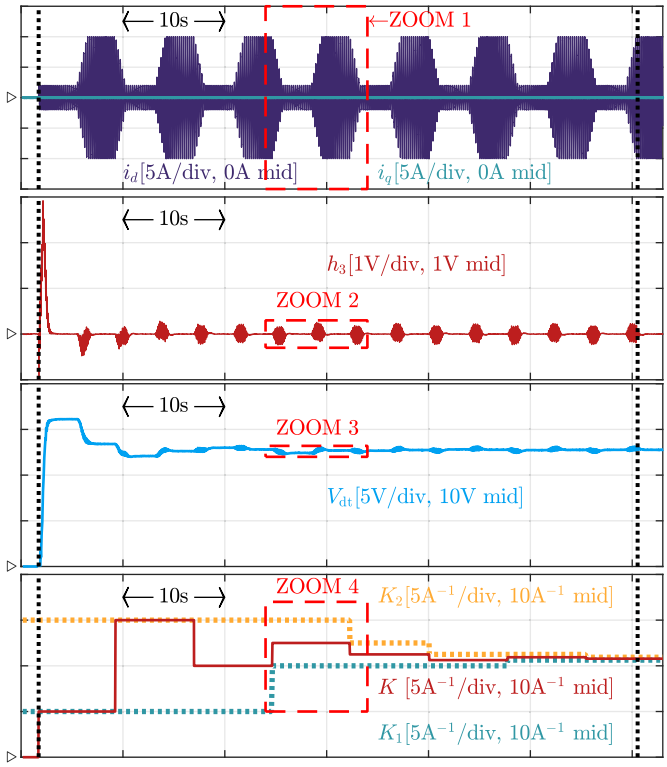

Fig. 14. Process of simultaneously identifying K and V_{dt} using Algorithm II. The dashed line on the left indicates the start of Algorithm II and the dashed line on the right indicates the end of Algorithm II.

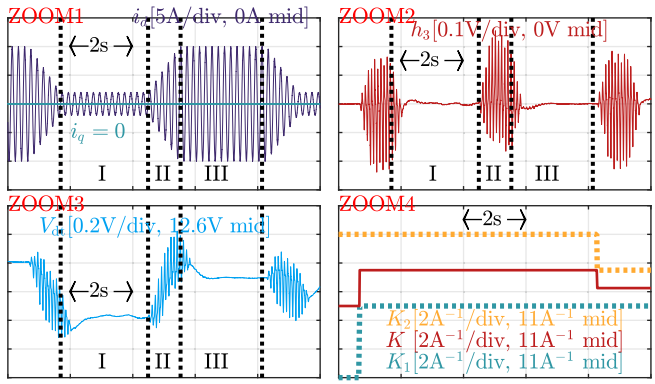

Fig. 15. Magnified view of Fig. 14.

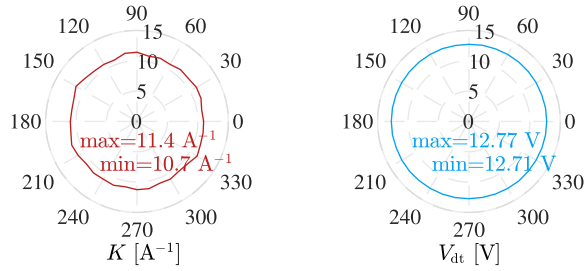

Fig. 16. Identification results of K and V_{dt} with different initial rotor positions.

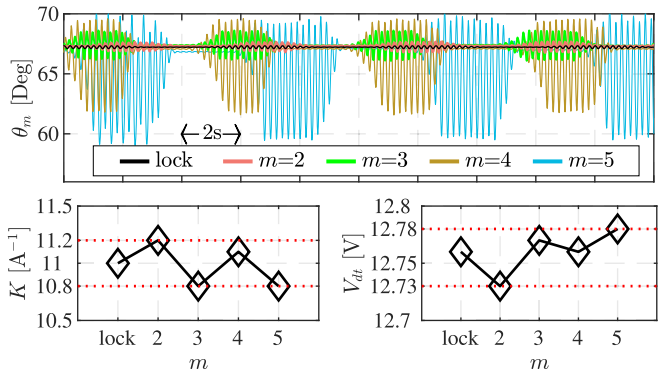

Fig. 17. Identification results with different m. θ_m is the rotor mechanical position.

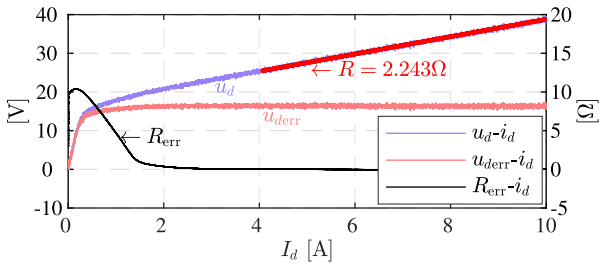

Fig. 18. Estimation of the DEVE on the *d*-axis using the method of nonlinear equivalent resistance during self-commission.

to K^*. As K converges to K^*, $V_{\rm dt}$ converges to $V_{\rm dt}^*$ at the same time using Algorithm I.

The magnified view of Fig. 14 is shown in Fig. 15. Fig. 15 represents one iteration of the Algorithm II. The current amplitude changes from mI to I and back to mI in this iteration. $K = 12.5\ \mathrm{A}^{-1}$. In region I, the current amplitude injected into the d-axis is I, and $V_{\rm dt}(K, I)$ is obtained by Algorithm I. In region II, the current amplitude rises from I to mI. In region III, the current amplitude injected into the d-axis is mI, and $V_{\rm dt}(K, mI)$ is obtained by Algorithm I. Substituting $V_{\rm dt}(K, I)$ and $V_{\rm dt}(K, mI)$ into (24) yields $f(K) < 0$. Then, $K_2 = K$, and the next round of iteration begins.

In Fig. 14, Algorithm II takes approximately 60 s to converge, and the final K satisfies the accuracy ξ under the aforementioned initial condition. Considering the property of the bisection method, the time complexity of the proposed method is $\log_2(n)$, where $n = (K_2 - K_1)/\xi$. Therefore, the time consumption is controllable and acceptable for self-commission.

As shown in Table VI, choosing different candidate intervals, the results obtained by Algorithm II are almost the same. The gap between the maximum and minimum values of K is $0.4\ \mathrm{A}^{-1}$, and $V_{\rm dt}$ is 0.03 V. This result proves that Algorithm II is independent of the initial candidate interval, as long as the interval satisfies Condition 2.

$I = 2$ A, $m = 5$, choosing different θ_d, the results of K and $V_{\rm dt}$ identified by Algorithm II are shown in Fig. 16. We experimentally verify that K and $V_{\rm dt}$ have consistent convergence values for different θ_d, although the sufficient condition (25) is not met for some cases of θ_d. In Fig. 16, the smallest K is $10.7\ \mathrm{A}^{-1}$, and the largest K is $11.4\ \mathrm{A}^{-1}$, while the smallest $V_{\rm dt}$ is 12.71 V, and the largest $V_{\rm dt}$ is 12.77 V.

TABLE VI
IDENTIFICATION RESULTS WITH DIFFERENT CANDIDATE INTERVALS

Interval	$K(\mathrm{A}^{-1})$	$V_{\rm dt}$(V)
[5, 15]	10.9	12.76
[5, 20]	11.0	12.77
[5, 30]	10.9	12.77
[5, 50]	10.6	12.78
[8, 16]	10.7	12.79
[8, 24]	10.7	12.78
[10, 15]	10.8	12.78
[10, 20]	10.8	12.78
[10, 30]	10.7	12.78

Due to the presence of many nonideal factors in practice, rotor position jitter is inevitable when injecting a sinusoidal current into the d-axis. The identification results generated by selecting different m are shown in Fig. 17. ("lock" indicates using the load motor to fix the rotor position of the test motor). Therefore, we demonstrate that the identification results are not significantly affected by moderate jitter.

In addition, there are many methods available to reduce the amplitude of rotor position jitter:

1) identifying a more accurate initial rotor position;
2) increasing actuator inertia;
3) choosing a relatively smaller m.

E. Comparison Experiment

Fig. 18 shows the DEVE estimation method used in [18], [19], [20], [21], [22], [23], and [24] during self-commission. This method considers that the DEVE is caused by a nonlinear equivalent resistance, whose value is influenced by the amplitude of fundamental phase currents. To keep the rotor at standstill, $i_q^* = 0$, and a slope current signal is injected into the d-axis. When the DEVE reaches the saturation region, u_d grows linearly with i_d, so the value of resistance on the d-axis can be obtained. Then, the DEVE on the d-axis, u_{derr}, can be calculated by subtracting the product of i_d and the value of resistance from u_d.

Three different two-parameter DEVE models based on the nonlinear equivalent resistance method are selected for comparison. These methods are commonly used prior to motor parameter identification during self-commission. The nonlinear equivalent resistance method is used to obtain the $V_{\rm dt}$ of the DEVE model in the *abc*-frame. Park and Sul [21] used a trapezoid wave to represent the transition region of the DEVE on each phase, while the shape parameter, K, is identified under the condition of motor rotation. Wang et al. [18] used a tanh model to represent the transition region, and the identification of K is similar to that of [21]. In [23], the transition region of the DEVE of each phase is obtained using coordinate transformation and recorded using a look-up table. The estimation results of the DEVE in the *abc*-frame by these methods are shown in Figs. 19 and 20. The blue curves in Figs. 19 and 20 are terminal voltage errors measured by an oscilloscope subtracting the on-stage voltages, $V_{\rm switch}$.

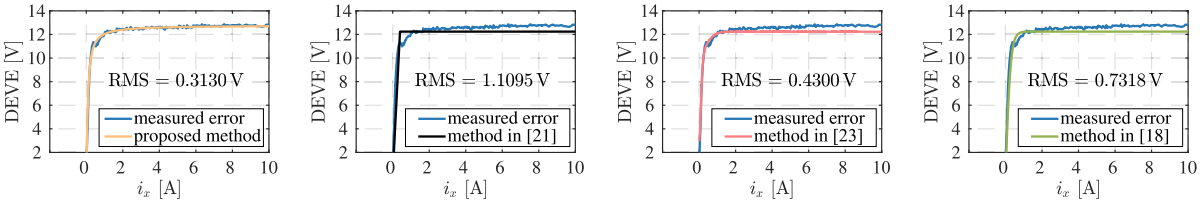

Fig. 19. Results of different methods to estimate the DEVE when the deadtime is set to 4 μs.

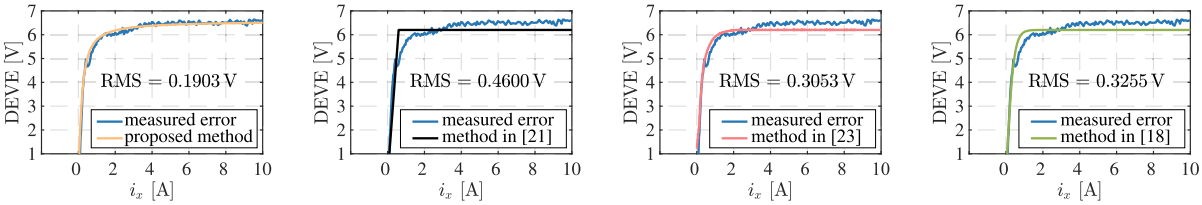

Fig. 20. Results of different methods to estimate the DEVE when the deadtime is set to 2 μs.

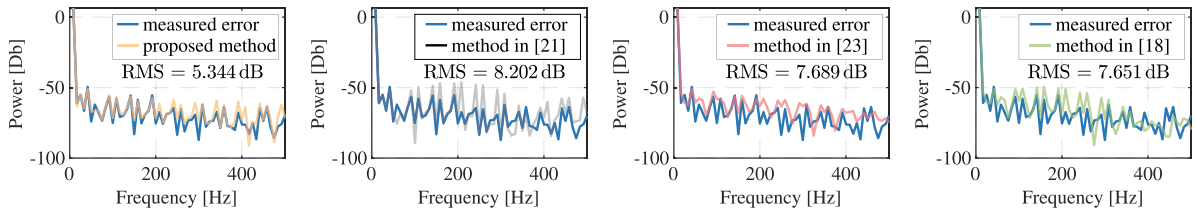

Fig. 21. Comparison of the a-phase current harmonic power.

These results were obtained on the experimental platform, as shown in Fig. 11. The method of obtaining the measured error is shown in Appendix D.

Fig. 19 shows the comparison of the estimated DEVEs in the *abc*-frame obtained by the following:

1) our method;
2) the method in [21];
3) the method in [23];
4) the method in [18].

For all comparisons, the practical DEVE is measured by an oscilloscope. We use root mean square (RMS) error to measure the distance between the estimated DEVE curve and the measured DEVE curve and the results are shown in Fig. 19. The DEVE estimated by the proposed method is closer to the measured DEVE. Additionally, Fig. 20 shows that the proposed method estimates the DEVE more accurately than the other methods when the deadtime is set to 2 μs.

Observing the measured DEVE shows that the real DEVE curve is not completely horizontal at the saturation region. Then, the estimated resistance on d-axis in Fig. 18 is slightly larger compared to the rated resistance in Table II. Therefore, the DEVEs estimated by [18], [21], and [23] are lower than the measured DEVEs in the saturation region. Additionally, among the four methods, only our method and the method in [23] estimate the DEVE completely under the condition that the motor is stationary. Therefore, the harmonics of the EMF do not affect the estimation results, and both are more accurate in the transition region. In addition, Wang et al. [23] needed to record the DEVE values of the transition region in a look-up table. Therefore, it requires more memory overhead than other methods.

Finally, the current harmonics after compensating for the DEVE using the four methods mentioned before are compared. The deadtime is set to 4 μs. The load motor rotates at 100 r/min, while the test motor is controlled in current mode and $i_q^* = 3$ A, $i_d^* = 0$ A. The THD of the a-phase current (selecting the first 100 harmonics) and the current harmonic power curve (generated by the "thd" function in MATLAB) are compared under the following conditions:

1) compensation by the method in [18];
2) compensation by the method in [21];
3) compensation by the method in [23];
4) compensation by our method;
5) compensation by the measured DEVE.

The results are shown in Table VII and Fig. 21. We also measure the distance between curves using RMS error and display the results in Fig. 21. To ensure a fair comparison, the SCDO is removed during the test, and the on-state voltages are all compensated by V_{switch} obtained in the datasheet. The THD of the current compensated by the measured DEVE is the minimum. Meanwhile, the THD of the current compensated by the proposed method in this article is the closest to the THD of the current compensated by the measured DEVE. Although the

TABLE VII
THD OF CURRENT ON a-PHASE USING DIFFERENT METHODS

Method	THD
No compensation	2.63%
Method proposed in [21]	0.60%
Method proposed in [18]	0.45%
Method proposed in [23]	0.33%
Our method	0.30%
Measured DEVE	0.28%

result of the current harmonic compensation of the proposed method is similar to [23], the harmonic power curve of the proposed method is closer to the measured error curve than [23]. This outcome illustrates that the DEVE estimated by our method is more accurate than the other estimations.

VI. CONCLUSION

In this article, a two-parameter arctan model is used to describe the DEVE, and an identification method is proposed during self-commission. Compared to previously proposed methods, this method simultaneously meets the following requirements.

1) Maintain the motor standstill at all times.
2) Overcoming the effect of the undesired harmonics of the EMF.
3) Obtain the DEVE in the *abc*-frame directly.
4) Simultaneously identify the two parameters to overcome the coupling problem.
5) Require no voltage sensor, no offline data processing, and no additional space to record data.

Experimentally, we demonstrate that the DEVE estimated by our method is more accurate than the results of existing state-of-the-art methods in the literature.

Nevertheless, the lower bound given by (25) in the proof of Theorem 2 is not sufficiently tight, resulting in a restricted range of theoretically available θ_d when identifying the parameters of the DEVE model. This limitation can be optimized in future work.

APPENDIX A
ANALYSIS OF THE STABILITY OF SCDO

The analysis is inspired by [27]. According to (5) and (6), the dynamic equations of the errors can be obtained as

$$\begin{cases} \dfrac{de_1}{dt} = -\dfrac{R}{L_d}e_1 - \dfrac{1}{L_d}e_3 - \dfrac{1}{L_d}U_{d\text{smo}} \\ \dfrac{de_3}{dt} = g_d U_{d\text{smo}} - F_d \end{cases} \tag{31}$$

$$\begin{cases} \dfrac{de_2}{dt} = -\dfrac{R}{L_q}e_2 - \dfrac{1}{L_q}e_4 - \dfrac{1}{L_q}U_{q\text{smo}} \\ \dfrac{de_4}{dt} = g_q U_{q\text{smo}} - F_q \end{cases} \tag{32}$$

where $e_1 = \widehat{i}_d - i_d$, $e_2 = \widehat{i}_q - i_q$, $e_3 = \widehat{f}_d - f_d$, and $e_4 = \widehat{f}_q - f_q$. The linear sliding-mode surface is chosen as

$$s_d = \widehat{i}_d - i_d, \quad s_q = \widehat{i}_q - i_q. \tag{33}$$

Then, an exponential reaching law is designed as

$$\frac{ds_i}{dt} = -k \cdot \text{sign}\,(s_i) - \lambda \cdot s_i, \qquad i = d, q. \tag{34}$$

According to (31), (32), (33), and (34), $U_{d\text{smo}}$ and $U_{q\text{smo}}$ can be obtained

$$\begin{cases} -\dfrac{R}{L_d}e_1 - \dfrac{1}{L_d}e_3 - \dfrac{1}{L_d}U_{d\text{smo}} = -k \cdot \text{sign}\,(e_1) - \lambda \cdot e_1 \\ -\dfrac{R}{L_q}e_2 - \dfrac{1}{L_q}e_4 - \dfrac{1}{L_q}U_{q\text{smo}} = -k \cdot \text{sign}\,(e_2) - \lambda \cdot e_2. \end{cases} \tag{35}$$

Considering e_3 and e_4 as the disturbances, the sliding-mode control function (7) can be derived.

To demonstrate the convergence of e_1, e_2, e_3, and e_4, the Lyapunov functions are designed as

$$\begin{cases} V_d = \dfrac{1}{2}{s_d}^2 \\ V_q = \dfrac{1}{2}{s_q}^2. \end{cases} \tag{36}$$

Then

$$\begin{aligned} \dot{V}_d &= -\frac{1}{L_d}e_1\left(Re_1 + e_3 + U_{d\text{smo}}\right) \\ &= -\frac{1}{L_d}\left[L_d\lambda {e_1}^2 + |e_1|\left(kL_d + e_3 \cdot \text{sign}\,(e_1)\right)\right]. \end{aligned} \tag{37}$$

If $k > |e_3|/L_d$, $\dot{V}_d < 0$. Similarly, if $k > |e_4|/L_q$, $\dot{V}_q < 0$. Therefore, e_1, e_2, $\dot{e}_1$, and $\dot{e}_2$ can converge to zero. Then, (31) and (32) can be converted to

$$\begin{cases} \dot{e}_3 + g_d e_3 + F_d = 0 \\ \dot{e}_4 + g_q e_4 + F_q = 0. \end{cases} \tag{38}$$

The positive values g_d and g_q are selected to ensure the convergence of e_3 and e_4, i.e.,

$$\widehat{f}_d \to f_d, \quad \widehat{f}_q \to f_q. \tag{39}$$

APPENDIX B
DISCRETE FORM OF SCDO

The discrete form of SCDO is

$$\begin{cases} \widehat{i}_d\,(K+1) = \left(1 - \dfrac{RT_c}{L_d}\right)\widehat{i}_d(K) + \dfrac{T_c}{L_d}u_d(K) \\ \qquad\qquad + T_c\dfrac{L_q}{L_d}\dfrac{p}{2}\omega_r(K)i_q(K) \\ \qquad\qquad - \dfrac{T_c}{L_d}\widehat{f}_d(K) - \dfrac{T_c}{L_d}U_{d\text{smo}}(K) \\ \widehat{f}_d\,(K+1) = \widehat{f}_d(K) + T_c g_d U_{d\text{smo}}(K) \\ U_{d\text{smo}}(K) = (L_d\lambda - R)\,e_1(K) + kL_d \cdot \text{sign}\,(e_1(K)) \\ e_1(K) = \widehat{i}_d(K) - i_d(K) \end{cases}, \tag{40}$$

$$\begin{cases} \widehat{i_q}(K+1) = \left(1 - \dfrac{RT_c}{L_q}\right)\widehat{i_q}(K) + \dfrac{T_c}{L_q}u_q(K) \\ \qquad -T_c\dfrac{L_d}{L_q}\dfrac{p}{2}\omega_r(K)i_d(K) - \dfrac{T_c\varphi_f}{L_q}\dfrac{p}{2}\omega_r(K) \\ \qquad -\dfrac{T_c}{L_q}\widehat{f_q}(K) - \dfrac{T_c}{L_q}U_{\text{qsmo}}(K) \\ \widehat{f_q}(K+1) = \widehat{f_q}(K) + T_c g_q U_{q\text{smo}}(K) \\ U_{q\text{smo}}(K) = (L_q\lambda - R)\, e_2(K) + kL_q \cdot \text{sign}\,(e_2(K)) \\ e_2(K) = \widehat{i_q}(K) - i_q(K) \end{cases}, \tag{41}$$

where T_c is the control period, and the initial values are chosen as $\widehat{f_d}(0) = 0$, $\widehat{f_q}(0) = 0$, $\widehat{i_d}(0) = i_d(0)$, and $\widehat{i_q}(0) = i_q(0)$.

Appendix C
Proof of Theorem 3

Theorem 3: In the closed interval $[K_1, K_2]$, $\partial v_3(K, I)/\partial K$ decreases monotonically with I when I satisfies the condition $I \geq 5/K_1$.

Proof: The proof is divided into three steps.

1) Step 1: Convert the proposition.

The expression of $\partial v_3(K, I)/\partial K$ is (16). Derive the partial derivative of $\partial v_3(K, I)/\partial K$ with respect to I, then

$$\frac{\partial}{\partial I}\frac{\partial v_3(K,I)}{\partial K} = \frac{8\pi}{\omega}\int_0^{\frac{\pi}{2\omega}} \frac{\sin(\omega t)\sin(3\omega t)\left[1 - K^2I^2\sin^2(\omega t)\right]}{\left[1 + K^2I^2\sin^2(\omega t)\right]^2}\text{d}t. \tag{42}$$

Let $K^2I^2 = a$, $a > 0$, and substituting t for ωt, then

$$m(a) = \frac{8\pi}{\omega^2}\int_0^{\frac{\pi}{2}} \frac{\sin(t)\sin(3t)\left[1 - a\cdot\sin^2(t)\right]}{\left[1 + a\cdot\sin^2(t)\right]^2}\text{d}t. \tag{43}$$

Therefore, the proposition is converted to that when $a \geq 25$, $m(a) < 0$.

2) Step 2: Drive the lower order upper bound of $m(a)$.

Let

$$\begin{cases} g(x) = \dfrac{x\left(1 - ax^2\right)}{\left(1 + ax^2\right)^2}, & 0 \leq x \leq 1 \\ h(x) = 3x - 4x^3, & 0 \leq x \leq 1. \end{cases} \tag{44}$$

Since

$$h\left(\sin(t)\right) = 3\sin(t) - 4\sin^3(t) = \sin(3t) \tag{45}$$

then

$$m(a) = \frac{8\pi}{\omega^2}\int_0^{\frac{\pi}{2}} h\left(\sin(t)\right) g\left(\sin(t)\right)\text{d}t. \tag{46}$$

In Fig. 22, the green areas represent the monotonically increasing intervals of $g(x)$ or $h(x)$, while the gray areas represent the monotonically decreasing intervals. The characteristic points are annotated on the coordinate axes.

The curves, $p(x)$ and $q(x)$ are constructed, as shown in Fig. 22. By alternately using constants, the order of $p(x)q(x)$ is lower than $g(x)h(x)$. The expressions of $p(x)$ and $q(x)$ are

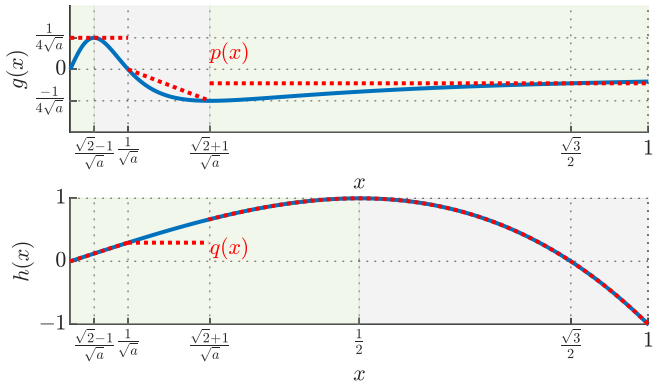

Fig. 22. Curves of $g(x)$, $p(x)$, $h(x)$, and $q(x)$ versus x.

$$p(x) = \begin{cases} \dfrac{1}{4\sqrt{a}}, & x \leq \dfrac{1}{\sqrt{a}} \\ -\dfrac{1}{4\sqrt{2}}x + \dfrac{1}{4\sqrt{2a}}, & \dfrac{1}{\sqrt{a}} < x \leq \dfrac{\sqrt{2}+1}{\sqrt{a}} \\ \dfrac{\sqrt{3}\left[1 - (3/4)\,a\right]}{2\left[1 + (3/4)\,a\right]^2}, & x > \dfrac{\sqrt{2}+1}{\sqrt{a}} \end{cases} \tag{47}$$

$$q(x) = \begin{cases} h\left(\dfrac{1}{\sqrt{a}}\right), & \dfrac{1}{\sqrt{a}} < x \leq \dfrac{(\sqrt{2}+1)}{\sqrt{a}} \\ h(x), & \text{others.} \end{cases} \tag{48}$$

The condition

$$a \geq 25 \tag{49}$$

can ensure that

$$\begin{cases} \min\left(h(x)\right) & = h\left(\dfrac{1}{\sqrt{a}}\right), \\ \dfrac{\sqrt{2}+1}{\sqrt{a}} & < \dfrac{\sqrt{3}}{2} \end{cases} \quad \text{when } x \in \left[\frac{1}{\sqrt{a}}, \frac{\sqrt{2}+1}{\sqrt{a}}\right] \tag{50}$$

and it is easy to infer that $g(x)h(x) < p(x)q(x)$.

Therefore, the lower order upper bound of $m(a)$ is

$$\begin{aligned} m(a) &< \frac{8\pi}{\omega^2}\int_0^{\frac{\pi}{2}} q\left(\sin(t)\right) p\left(\sin(t)\right)\text{d}t \\ &= \frac{8\pi}{\omega^2}\left[m_1(a) + m_2(a)\right] \end{aligned} \tag{51}$$

where

$$m_1(a) = \frac{\sqrt{3}\left[1 - (3/4)\,a\right]}{2\left[1 + (3/4)\,a\right]^2} \times \underbrace{\int_{\arcsin\frac{\sqrt{2}+1}{\sqrt{a}}}^{\frac{\pi}{2}} \sin(3t)\text{d}t}_{\widetilde{m_1}(a)} \tag{52}$$

and

$$m_2(a) = \Bigg[\underbrace{\frac{1}{4\sqrt{a}} \int_0^{\arcsin \frac{1}{\sqrt{a}}} h\left(\sin(t)\right) \mathrm{d}t}_{T_1(a)} + \underbrace{\frac{1}{4\sqrt{2}} \int_{\arcsin \frac{1}{\sqrt{a}}}^{\arcsin \frac{\sqrt{2}+1}{\sqrt{a}}} h\left(\frac{1}{\sqrt{a}}\right)\left(-\sin(t)+\frac{1}{\sqrt{a}}\right) \mathrm{d}t}_{T_2(a)} \Bigg]. \tag{53}$$

3) Step 3: Proof $m_1(a) < 0$, $m_2(a) < 0$ when $a \geq 25$.

When $a > 25$, $\sqrt{3}[1-(3/4)a]/2[1+(3/4)a]^2 < 0$. $\widetilde{m_1}(a)$ increases monotonically with a, and $\widetilde{m_1}(25) > 0$. Therefore, if $a \geq 25$, $\widetilde{m_1}(a) > 0$, $m_1(a) < 0$.

Then, we need to prove $m_2(a) < 0$.

First, simplify $T_1(a)$. In the integral interval

$$h\left(\sin(t)\right) = 3\sin(t) - 4\sin^3(t) < 3\sin(t) \tag{54}$$

then

$$\begin{aligned} T_1(a) &< \frac{3}{4\sqrt{a}} \int_0^{\arcsin \frac{1}{\sqrt{a}}} \sin(t)\mathrm{d}t \\ &= \frac{3}{4a}\left(\sqrt{a} - \sqrt{a-1}\right). \end{aligned} \tag{55}$$

The simplification uses the formula

$$\cos\left(\arcsin(x)\right) = \sqrt{1-x^2}. \tag{56}$$

Next, simplify $T_2(a)$

$$\begin{aligned} h\left(\frac{1}{\sqrt{a}}\right) &= 3\frac{1}{\sqrt{a}} - 4\left(\frac{1}{\sqrt{a}}\right)^3 \\ &= \frac{1}{\sqrt{a}}\left(3 - \frac{4}{a}\right). \end{aligned} \tag{57}$$

Then

$$\begin{aligned} T_2(a) &= \frac{1}{4\sqrt{2a}}\left(3-\frac{4}{a}\right) \int_{\arcsin \frac{1}{\sqrt{a}}}^{\arcsin \frac{\sqrt{2}+1}{\sqrt{a}}} \left(-\sin(t) + \frac{1}{\sqrt{a}}\right) \mathrm{d}t \\ &= \frac{1}{4a\sqrt{2}}\left(3-\frac{4}{a}\right)\left[\left(\sqrt{a-\left(3+2\sqrt{2}\right)} - \sqrt{a-1}\right)\right. \\ &\quad \left. + \left(\arcsin\left(\frac{\sqrt{2}+1}{\sqrt{a}}\right) - \arcsin\left(\frac{1}{\sqrt{a}}\right)\right)\right]. \end{aligned} \tag{58}$$

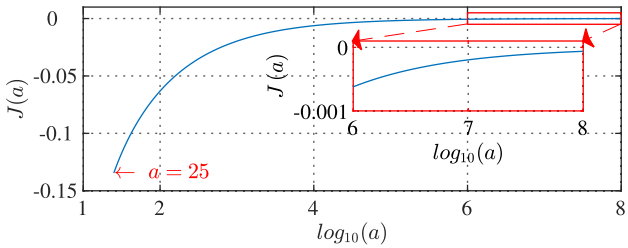

Fig. 23. Numerical simulation result of $J(a)$ when $a \geq 25$.

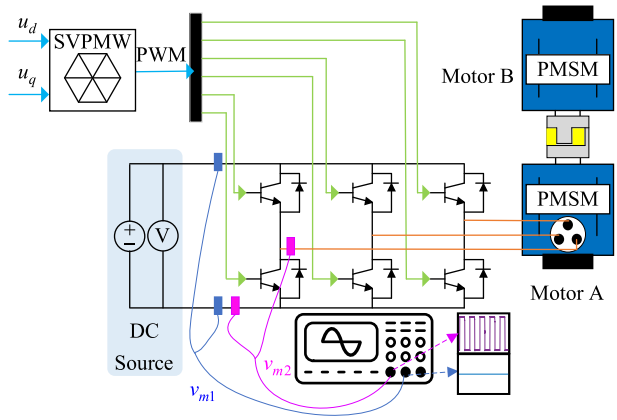

Fig. 24. Measurement diagram.

Merge (55) and (58), then It is easy to find that $J(+\infty) = 0$. $J(a)$ is a continuous univariate function without integral terms when $a \geq 25$. As shown in Fig. 23, it is easy to verify that $J(a) < 0$ and $J(+\infty) = 0$ using the numerical approach. Then, $m_2(a) = T_1(a) + T_2(a) \leq 0$.

Thus, $m(a) < 0$. $\partial v_3(K, I)/\partial K$ decreases monotonically with I when $a \geq 25$, i.e., $I \geq 5/K_1$. □

APPENDIX D
METHOD OF OBTAINING THE MEASURED ERROR

The diagram is shown in Fig. 24. The principle of measurement is to maintain a constant current in the three phases and then measure the difference between the output voltage and the input voltage of the VSI. To ensure that the test results are meaningful in comparative experiments, the VSI is connected to the tested motor in Fig. 11 for DEVE testing. In this way, all error curves are obtained in the same environment.

Taking the a-phase in the abc-frame as an example for testing, the two voltage probes of the oscilloscope are connected to the positive and negative terminals of the dc source, the negative terminal of the dc source and the a-phase output terminal of the

$$\begin{aligned} &T_1(a) + T_2(a) \\ &< \frac{1}{4a}\underbrace{\left\{3\left(\sqrt{a}-\sqrt{a-1}\right) + \frac{\left(3-\frac{4}{a}\right)}{\sqrt{2}}\left[\left(\sqrt{a-\left(3+2\sqrt{2}\right)} - \sqrt{a-1}\right) + \left(\arcsin\left(\frac{\sqrt{2}+1}{\sqrt{a}}\right) - \arcsin\left(\frac{1}{\sqrt{a}}\right)\right)\right]\right\}}_{J(a)}. \end{aligned} \tag{59}$$

VSI. Using Motor B in Fig. 24 to control the alignment the d-axis of the test motor's rotor with the stator's a-phase. Set the voltage commands in the controller, $u_q = 0$, and vary u_d to finish the test.

When the rotor is stationary, the PWM duty cycle calculated by the space vector pulse width modulation (SVPWM) module, D_a, D_b, D_c, remains constant. (If current closed-loop control is adopted, the PWM duty cycle and the measured voltage v_{m2} will jitter on the oscilloscope due to the effect of the closed-loop control. In that case, the PWM duty cycle must also be measured simultaneously.) Due to the presence of inductance in the motor, it is necessary to wait for the current values to reach a steady state before obtaining i_a from the feedback current signal. Then, obtain v_{m1} and v_{m2} from the oscilloscope. Notably, v_{m2} is a square-wave like signal. Then,

$$\mathrm{DEVE}_{\mathrm{meas}}\left(i_a\right) = D_a \cdot \overline{v_{m1}} - \overline{v_{m2}} - V_{\mathrm{switch}}\left(i_a\right) \tag{60}$$

where V_{switch} can be obtained in the datasheet, and $\overline{v_{m1}}$ and $\overline{v_{m2}}$ represent the averages of v_{m1} and v_{m2} in a control period. By repeating the abovementioned test, the measured error in Figs. 19 and 20 can be obtained.

REFERENCES

[1] S. A. Odhano, P. Pescetto, H. A. A. Awan, M. Hinkkanen, G. Pellegrino, and R. Bojoi, "Parameter identification and self-commissioning in ac motor drives: A technology status review," *IEEE Trans. Power Electron.*, vol. 34, no. 4, pp. 3603–3614, Apr. 2019.

[2] G. Liu, B. Chen, K. Wang, and X. Song, "Selective current harmonic suppression for high-speed PMSM based on high-precision harmonic detection method," *IEEE Trans. Ind. Informat.*, vol. 15, no. 6, pp. 3457–3468, Jun. 2019.

[3] Z. Tang and B. Akin, "Suppression of dead-time distortion through revised repetitive controller in PMSM drives," *IEEE Trans. Energy Convers.*, vol. 32, no. 3, pp. 918–930, Sep. 2017.

[4] S.-H. Hwang and J.-M. Kim, "Dead time compensation method for voltage-fed PWM inverter," *IEEE Trans. Energy Convers.*, vol. 25, no. 1, pp. 1–10, Mar. 2010.

[5] N. Urasaki, T. Senjyu, K. Uezato, and T. Funabashi, "Adaptive dead-time compensation strategy for permanent magnet synchronous motor drive," *IEEE Trans. Energy Convers.*, vol. 22, no. 2, pp. 271–280, Jun. 2007.

[6] S.-Y. Kim and S.-Y. Park, "Compensation of dead-time effects based on adaptive harmonic filtering in the vector-controlled ac motor drives," *IEEE Trans. Ind. Electron.*, vol. 54, no. 3, pp. 1768–1777, Jun. 2007.

[7] S.-Y. Kim, W. Lee, M.-S. Rho, and S.-Y. Park, "Effective dead-time compensation using a simple vectorial disturbance estimator in pmsm drives," *IEEE Trans. Ind. Electron.*, vol. 57, no. 5, pp. 1609–1614, May 2010.

[8] M. Seilmeier, C. Wolz, and B. Piepenbreier, "Modelling and model based compensation of non-ideal characteristics of two-level voltage source inverters for drive control application," in *Proc. Int. Elect. Drives Prod. Conf.*, 2011, pp. 17–22.

[9] M. Stender, O. Wallscheid, and J. Böcker, "Comparison of gray-box and black-box two-level three-phase inverter models for electrical drives," *IEEE Trans. Ind. Electron.*, vol. 68, no. 9, pp. 8646–8656, Sep. 2021.

[10] T. Mannen and H. Fujita, "Dead-time compensation method based on current ripple estimation," *IEEE Trans. Power Electron.*, vol. 30, no. 7, pp. 4016–4024, Jul. 2015.

[11] Z. Zhang and L. Xu, "Dead-time compensation of inverters considering snubber and parasitic capacitance," *IEEE Trans. Power Electron.*, vol. 29, no. 6, pp. 3179–3187, Jun. 2014.

[12] P. Shan, M. Yang, X. Li, C. Shang, J. Long, and D. Xu, "Online inverter nonlinearity compensation method based on current injection," in *Proc. Int. Conf. Elect. Mach. Syst.*, 2021, pp. 1911–1916.

[13] J. Chen, J. Mei, X. Yuan, Y. Zuo, J. Zhu, and C. H. T. Lee, "Online adaptation of two-parameter inverter model in sensorless motor drives," *IEEE Trans. Ind. Electron.*, vol. 69, no. 10, pp. 9860–9871, Oct. 2022.

[14] P. Wang, K. Lin, X. Zhang, S. Wang, J. Ai, and M. Lin, "An online estimation method for both stator inductance and rotor flux linkage of SPMSM without dead-time influence," *IEEE J. Emerg. Sel. Topics Power Electron.*, vol. 10, no. 2, pp. 1627–1638, Apr. 2022.

[15] K. Liu, J. Feng, S. Guo, L. Xiao, and Z.-Q. Zhu, "Identification of flux linkage map of permanent magnet synchronous machines under uncertain circuit resistance and inverter nonlinearity," *IEEE Trans. Ind. Informat.*, vol. 14, no. 2, pp. 556–568, Feb. 2018.

[16] D.-M. Park and K.-H. Kim, "Parameter-independent online compensation scheme for dead time and inverter nonlinearity in iPMSM drive through waveform analysis," *IEEE Trans. Ind. Electron.*, vol. 61, no. 2, pp. 701–707, Feb. 2014.

[17] J.-H. Lee and S.-K. Sul, "Inverter nonlinearity compensation through deadtime effect estimation," *IEEE Trans. Power Electron.*, vol. 36, no. 9, pp. 10684–10694, Sep. 2021.

[18] Q. Wang, G. Wang, N. Zhao, G. Zhang, Q. Cui, and D. Xu, "An impedance model-based multiparameter identification method of pmsm for both offline and online conditions," *IEEE Trans. Power Electron.*, vol. 36, no. 1, pp. 727–738, Jan. 2021.

[19] G. Wang et al., "Self-commissioning of permanent magnet synchronous machine drives at standstill considering inverter nonlinearities," *IEEE Trans. Power Electron.*, vol. 29, no. 12, pp. 6615–6627, Dec. 2014.

[20] M. El-Daleel and A. Mahgoub, "Accurate and simple improved lookup table compensation for inverter dead time and nonlinearity compensation," in *Proc. Int. Middle East Power Syst. Conf.*, 2017, pp. 1358–1361.

[21] Y. Park and S.-K. Sul, "A novel method utilizing trapezoidal voltage to compensate for inverter nonlinearity," *IEEE Trans. Power Electron.*, vol. 27, no. 12, pp. 4837–4846, Dec. 2012.

[22] D. Pengcheng, X. Dianguo, W. Bo, and Y. Yong, "Offline parameter identification strategy of permanent magnet synchronous motor considering the inverter nonlinearities," in *Proc. Int. Conf. Elect. Mach. Syst.*, 2022, pp. 1–5.

[23] Q. Wang et al., "An offline parameter self-learning method considering inverter nonlinearity with zero-axis voltage," *IEEE Trans. Power Electron.*, vol. 36, no. 12, pp. 14098–14109, Dec. 2021.

[24] Q. Wang, G. Zhang, G. Wang, C. Li, and D. Xu, "Offline parameter self-learning method for general-purpose PMSM drives with estimation error compensation," *IEEE Trans. Power Electron.*, vol. 34, no. 11, pp. 11103–11115, Nov. 2019.

[25] V. Varvolik, D. Prystupa, G. Buticchi, S. Peresada, M. Galea, and S. Bozhko, "Inverter nonlinearity effects on self-commissioning of synchronous reluctance drives," in *Proc. Int. Conf. Elect. Mach. Syst.*, 2021, pp. 1792–1797.

[26] C. Lian, F. Xiao, S. Gao, and J. Liu, "Load torque and moment of inertia identification for permanent magnet synchronous motor drives based on sliding mode observer," *IEEE Trans. Power Electron.*, vol. 34, no. 6, pp. 5675–5683, Jun. 2019.

[27] X. Zhang, B. Hou, and Y. Mei, "Deadbeat predictive current control of permanent-magnet synchronous motors with stator current and disturbance observer," *IEEE Trans. Power Electron.*, vol. 32, no. 5, pp. 3818–3834, May 2017.

[28] Y. Zuo, J. Mei, C. Jiang, and C. H. T. Lee, "Digital implementation of deadbeat-direct torque and flux control for permanent magnet synchronous machines in the M–T reference frame," *IEEE Trans. Power Electron.*, vol. 36, no. 4, pp. 4610–4621, Apr. 2021.

[29] G. Feng, C. Lai, K. Mukherjee, and N. C. Kar, "Current injection-based online parameter and VSI nonlinearity estimation for PMSM drives using current and voltage DC components," *IEEE Trans. Power Electron.*, vol. 2, no. 2, pp. 119–128, Jun. 2016.

[30] Y. Zhang, J. Jin, and L. Huang, "Model-free predictive current control of PMSM drives based on extended state observer using ultralocal model," *IEEE Trans. Ind. Electron.*, vol. 68, no. 2, pp. 993–1003, Feb. 2021.

Danqi Xiang (Student Member, IEEE) received the B.S. and M.S. degrees in mechanical engineering in 2017 and 2020, respectively, from the Huazhong University of Science and Technology, Wuhan, China, where he is currently working toward the Ph.D. degree in mechanical engineering with the School of Mechanical Science and Engineering.

His current research interests include motion control, nonlinear control, and PMSM servo system.

Jianzhong Yang received the Ph.D. degree in mechanical engineering from the Huazhong University of Science and Technology, Wuhan, China, in 2006.

He is currently a Professor with the National NC System Engineering Research Center, Huazhong University of Science and Technology. His research interests include intelligent technology of CNC system, advanced control theory, intelligent automation system, and robot technology.

Yong Hao (Student Member, IEEE) received the B.S. degree in mechanical engineering in 2019 from the Huazhong University of Science and Technology, Wuhan, China, where he is currently working toward the Ph.D. degree in mechanical engineering with the School of Mechanical Science and Engineering.

His current research interests include PMSM servo system and NC rotary table direct drive rotary feeding system.

Guangda Xu received the bachelor's and Ph.D. degrees in mechanical engineering from School of Mechanical Science and Engineering (MSE), Huazhong University of Sciences and Technology (HUST), Wuhan, China, in June 2013 and December 2018, respectively.

After graduating with the Ph.D., he was a Postdoctoral Researcher with HUST. He became a Lecturer with MSE, HUST, in October 2022. His current research interests include intelligent CNC system, servo control, signal processing and big data intelligence, fusion modeling of big data model, and mechanism model.